Introduction to Downhole Logging

Alberto Malinverno

Well Logging Principles and Applications
G9947 - Seminar in Marine Geophysics
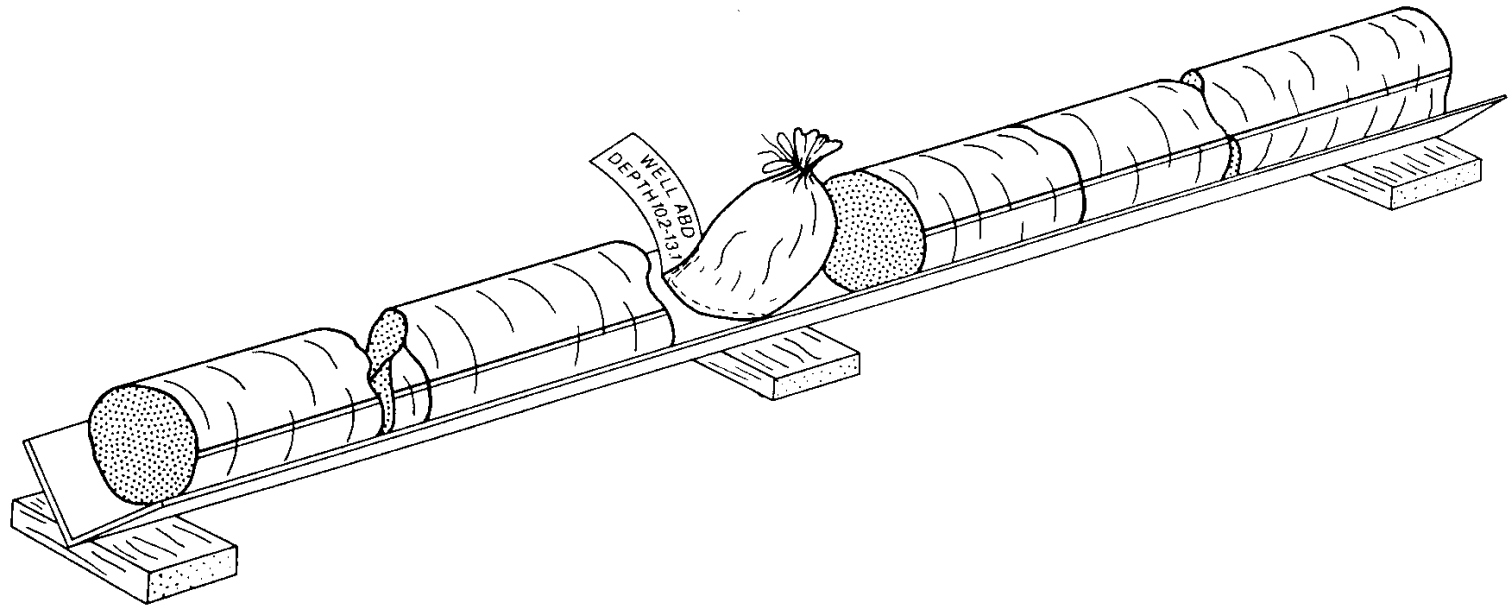Spring 2008

Fig. 3.2 Core pieces fitted together on a length of angle-iron. A rubbly section is contained in the bag. The parallel lines marked on the core, which would be in contrasting colours, indicate the way up.

in si·tu

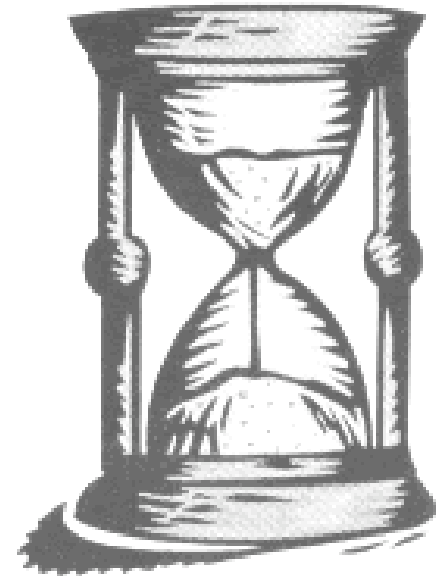in the natural or original position or place

Pronunciation: (")in-'sI-(")tü, -'si-, -(")tyü *also* -'sE-, -(")chü

Function: adverb or adjective
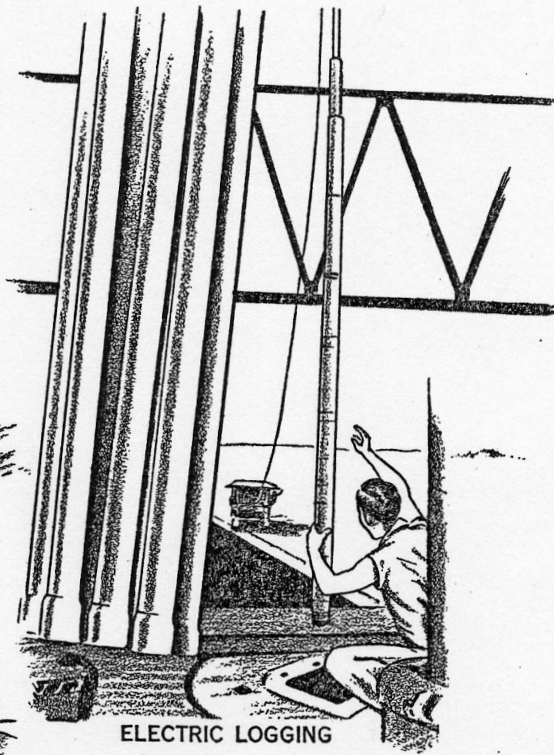
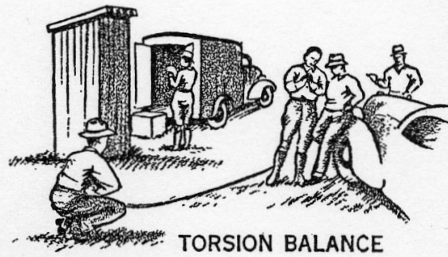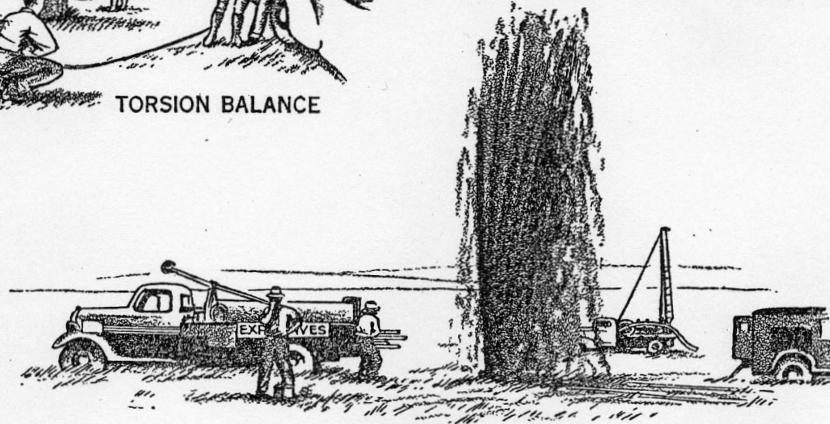Etymology: Latin, in position

Date: 1740

GEOPHYSICS AT WORK
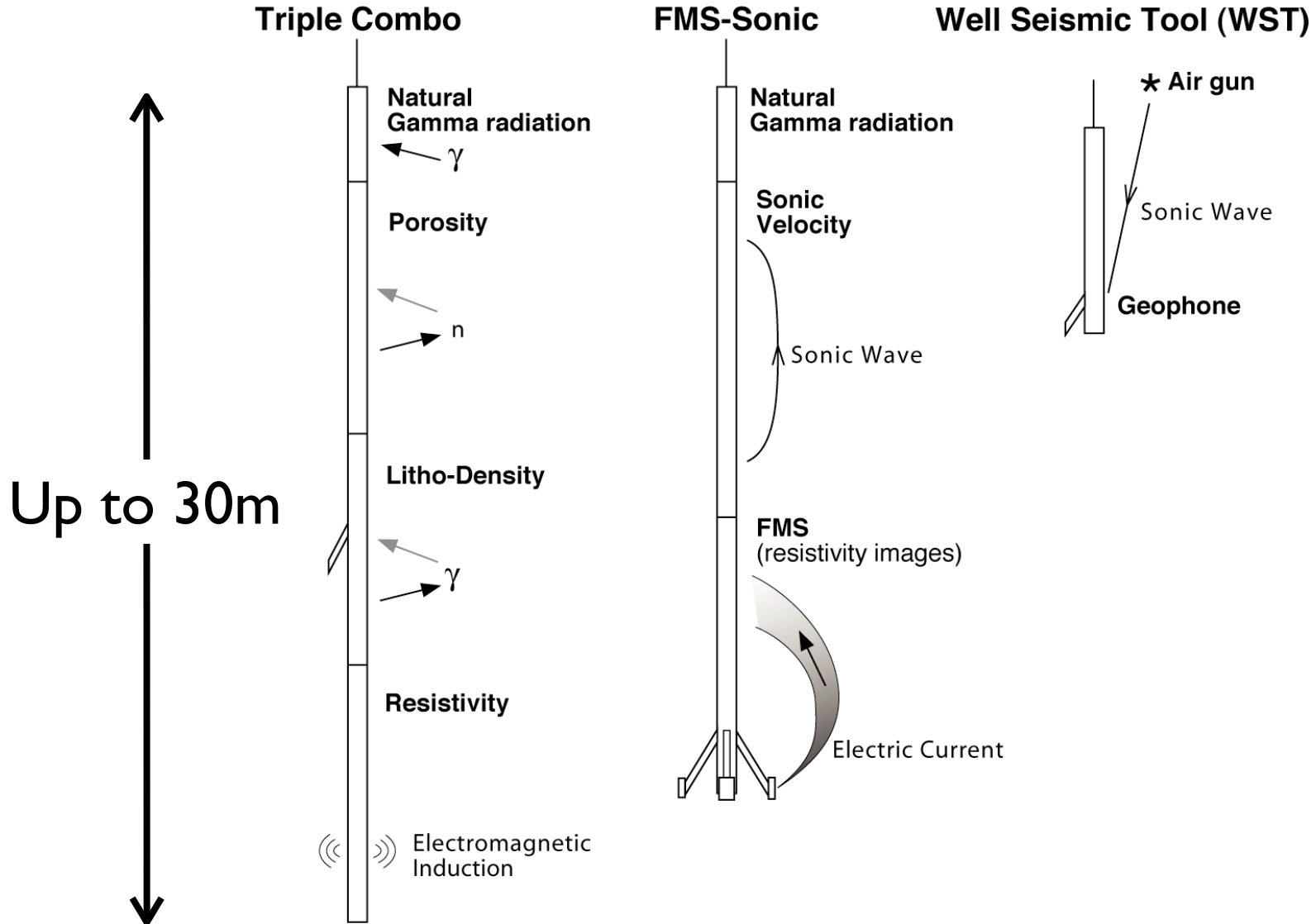

MAGNETOMETER

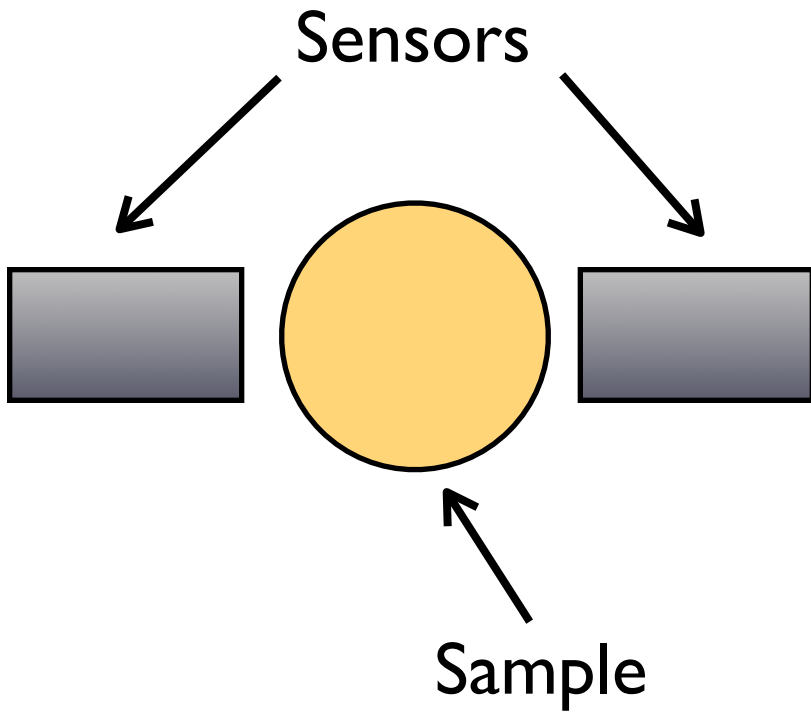**ELECTRIC LOGGING**

TORSION BALANCE

SEISMOGRAPH

Many geophysical methods are used in attempting to determine the attitude, character, and contents of rocks beneath the surface. These sketches show men busy at some of those in common use.
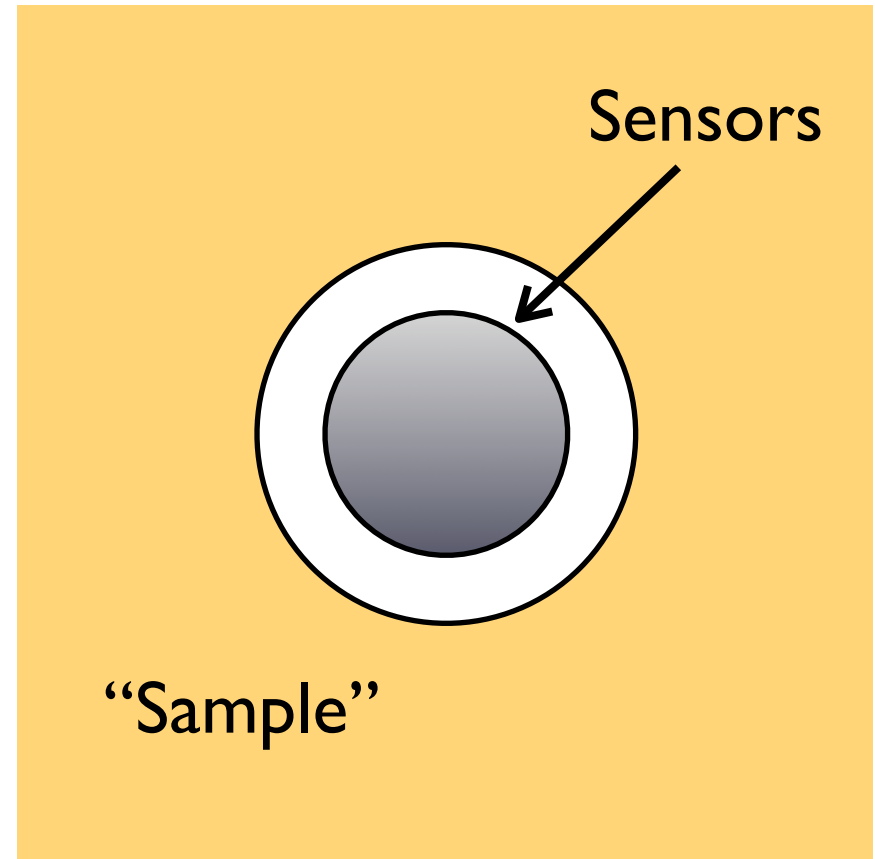
Wireline tool strings

Triple Combo

Natural Gamma radiation

γ

Porosity

n

Litho-Density

γ

Resistivity

Electromagnetic Induction

Up to 30m

FMS-Sonic

Natural Gamma radiation

Sonic Velocity

Sonic Wave

FMS (resistivity images)

Electric Current

Well Seismic Tool (WST)

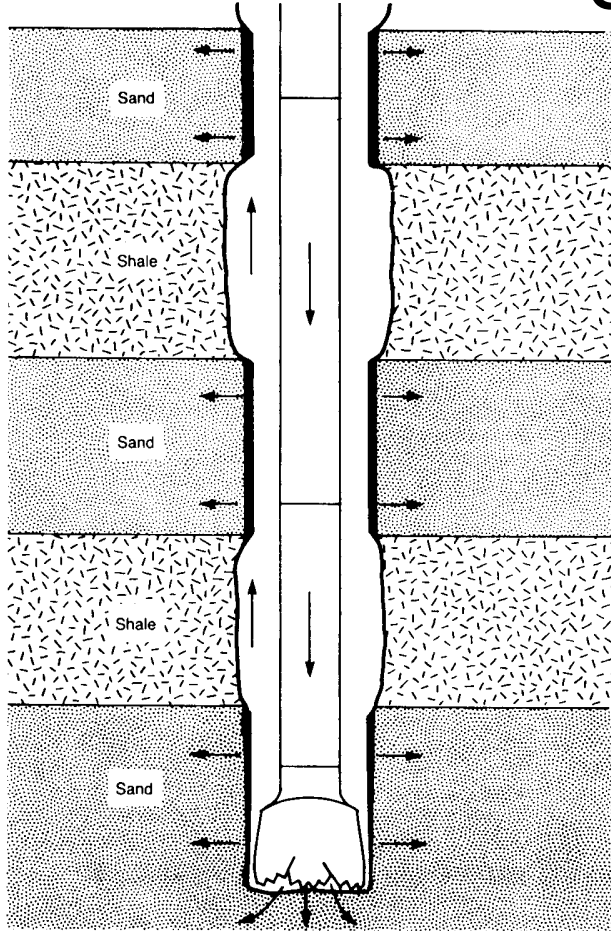★ Air gun

Sonic Wave

Geophone

Measurements on core samples

Sensors

Sample

Measurements in the borehole

Sensors

"Sample"

Degradation of the formation during and after drilling. Overpressured mud is indicated to be invading porous and permeable sand formations with the formation of a mudcake. The mud circulation also causes borehole washout in the shale zones. From Dewan.[1]
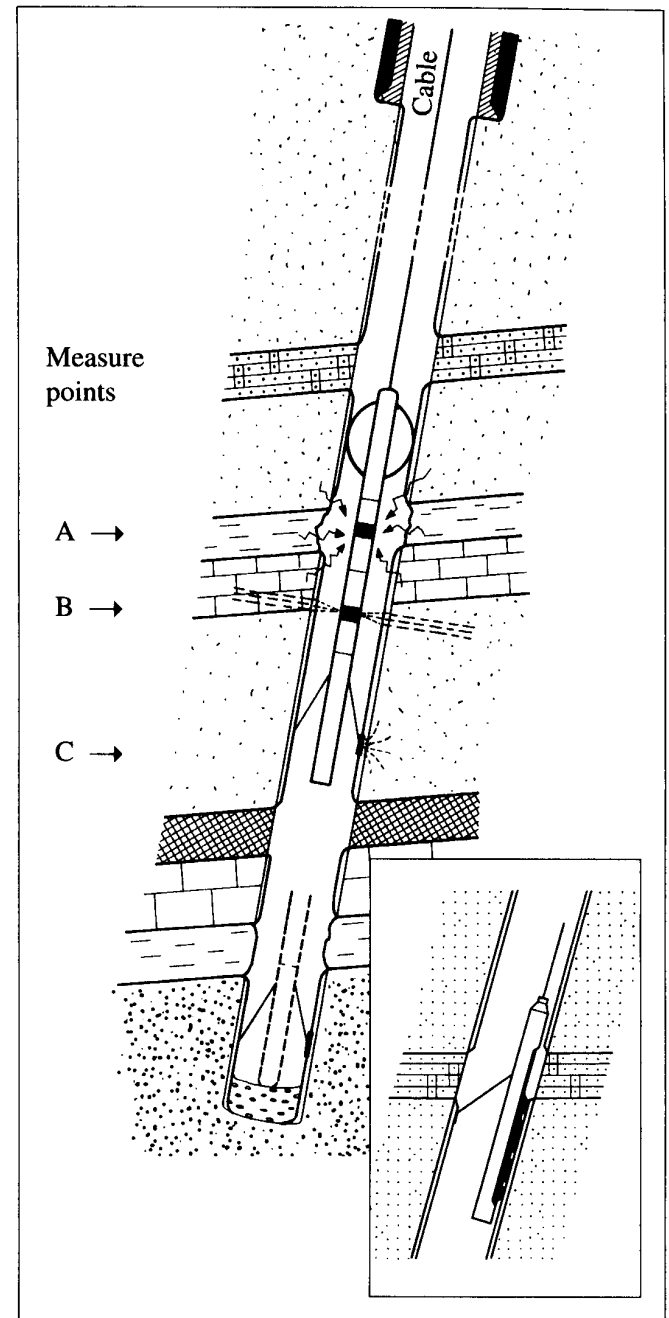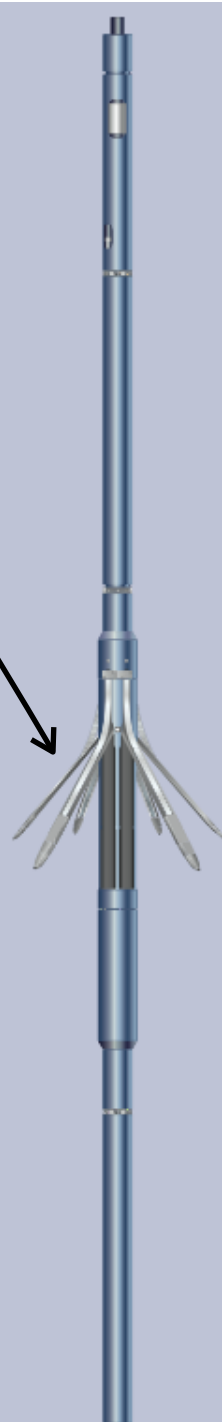
6-arm caliper

Fig. 1.1 Logging tools in the wellbore.

- Nuclear Logs
  - Natural gamma ray
  - Density
  - Neutron
  - Thermal neutron capture
- Sonic
- Electrical / magnetic
- Imaging
- Vertical seismic profile (VSP)
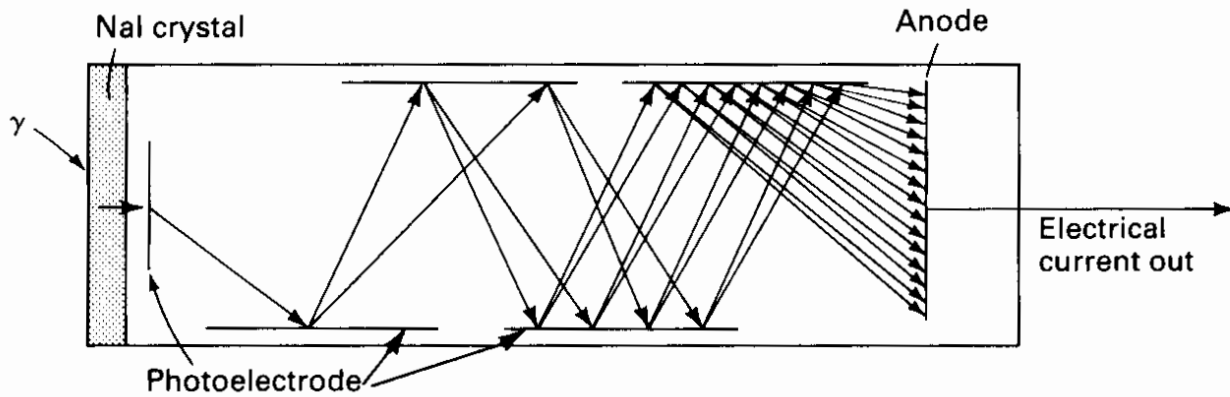- Logging While Drilling
- Examples

Figure 7.4 Schematic of a scintillation counter. An incident gamma ray on the scintillation crystal of NaI causes the crystal to emit a photon, which then causes the photoelectrode to emit electrons. The number of electrons is multiplied as each strikes a series of electrodes, finally being collected by an anode where the consequent current is proportional to the energy of the incident gamma ray.

- Gamma ray ≈ shale indicator
- Gamma ray log

  GR(API) = 4Th(ppm) + 8U(ppm) + 16K(%)

- Compensated gamma ray

  CGR(API) = 4Th(ppm) + 16K(%)

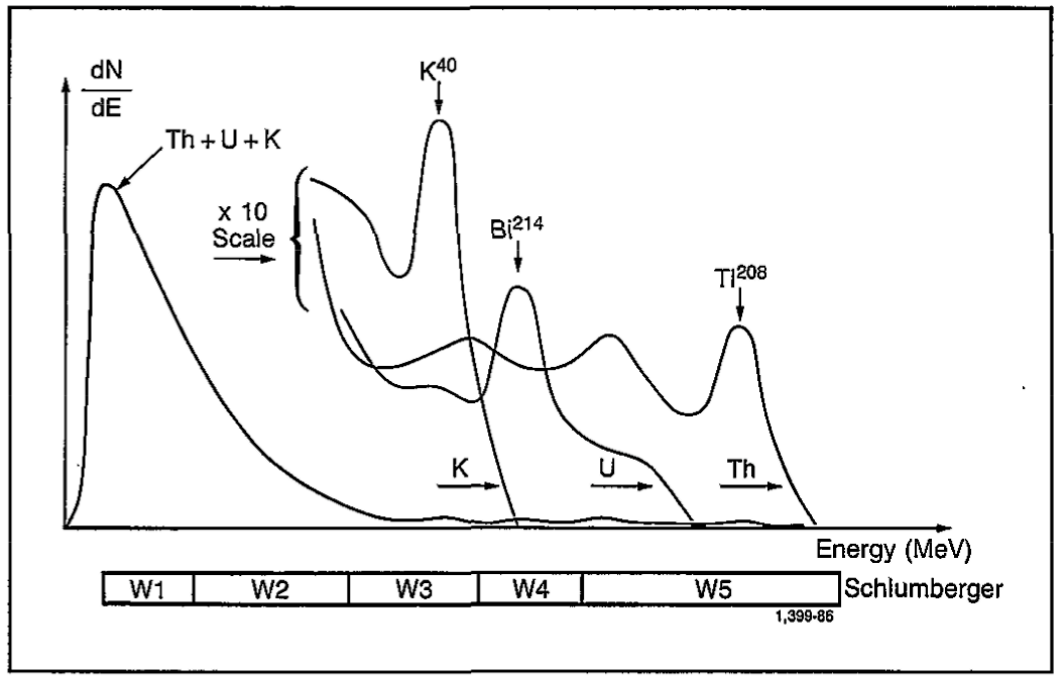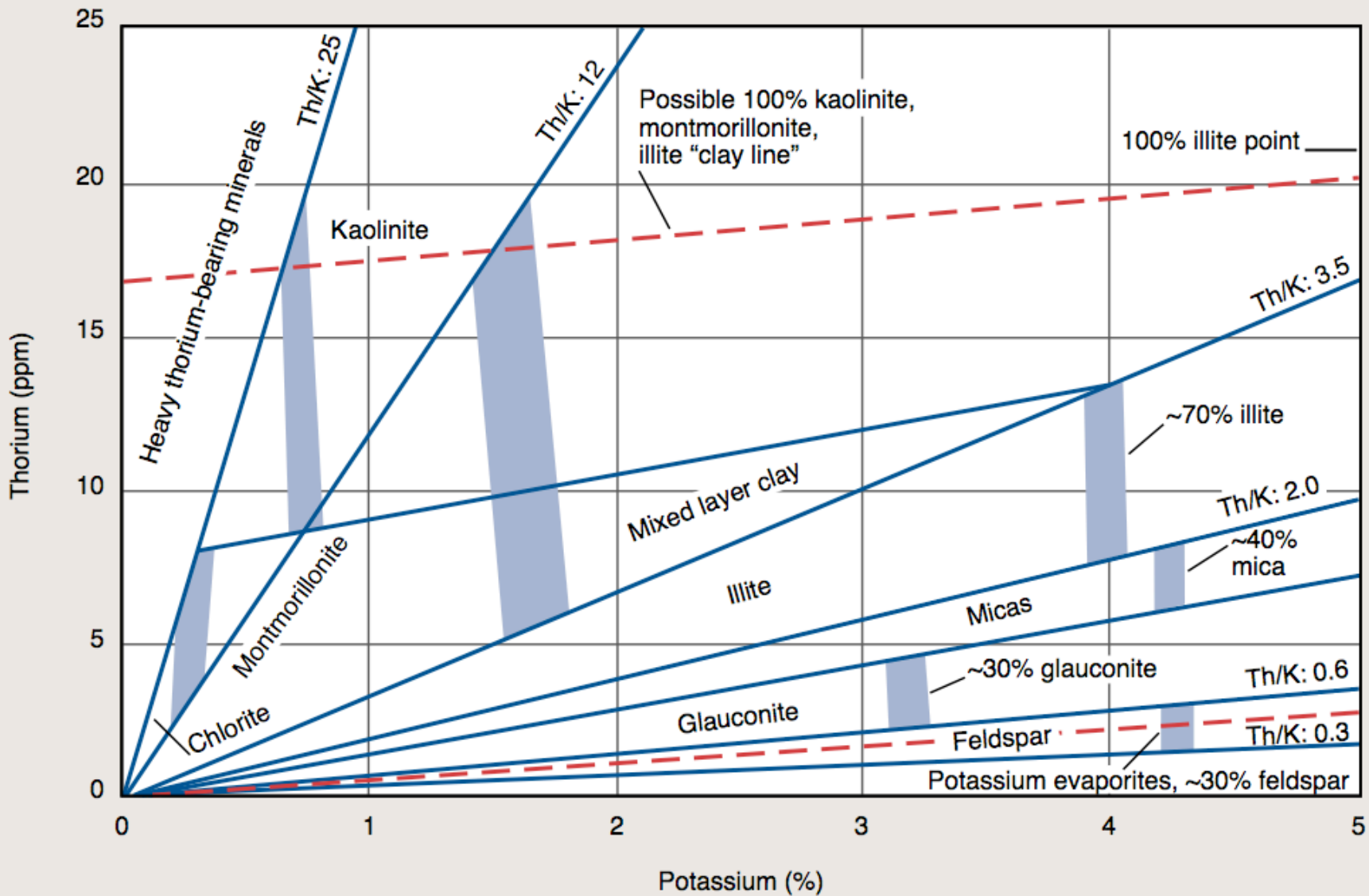- CGR ignores U, which is not always associated with shales

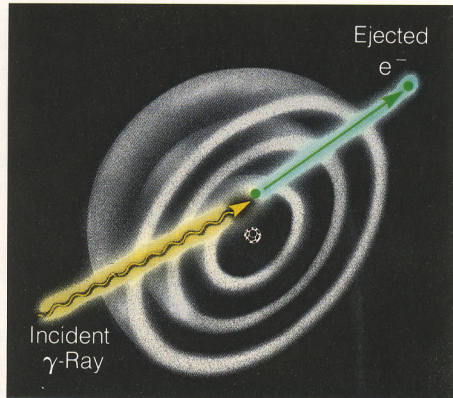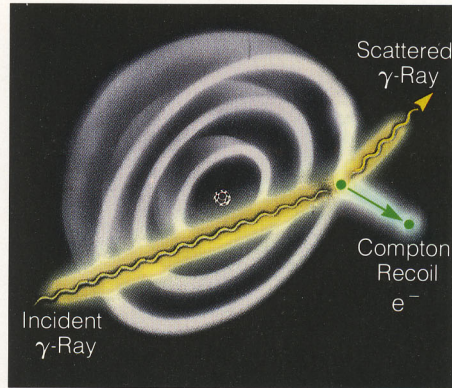Fig. 3-9—Potassium, thorium, and uranium response curves (NaI crystal detector).

* Mark of Schlumberger
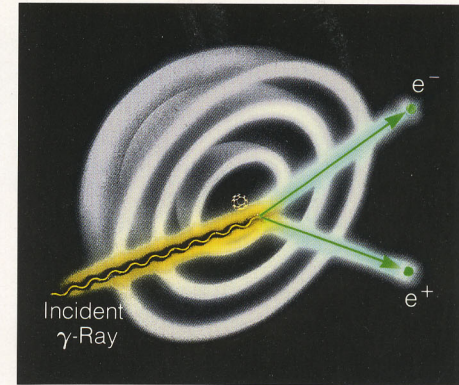© Schlumberger

Photoelectric absorption

□ *In photoelectric absorption, a low-energy γ-ray disappears as it collides with an atom, ejecting an electron from orbit.*
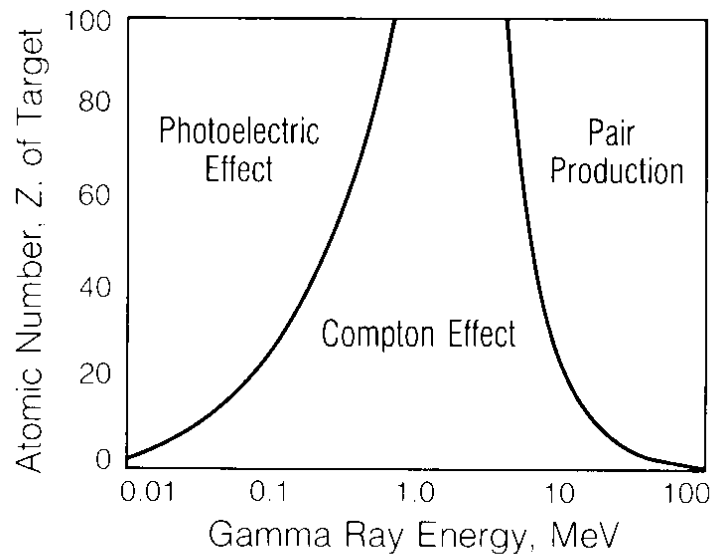
Compton scattering

□ *In Compton scattering, the γ-ray changes course when it bounces off an orbital electron.*

Pair production

□ *In pair production, a γ-ray collides with a nucleus, disappears, and converts into an electron and a positron. If the γ-ray has enough energy, it knocks an electron out of the innermost shell.*

gamma ray energy ⟶

Atomic Number, Z. of Target

Photoelectric Effect

Pair Production

Compton Effect

Gamma Ray Energy, MeV

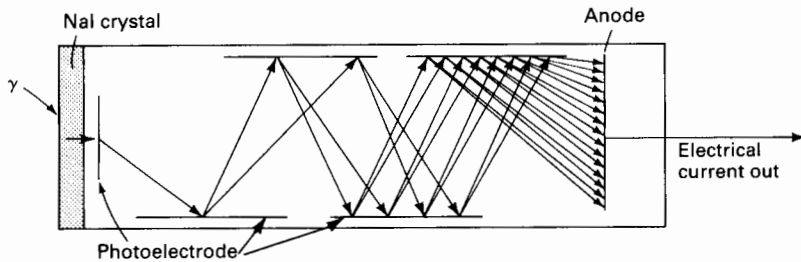NaI crystal

Anode

γ

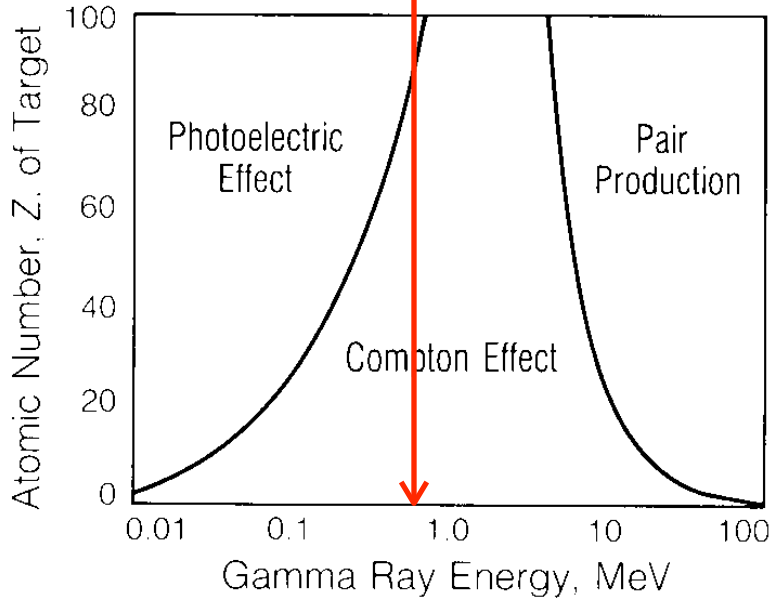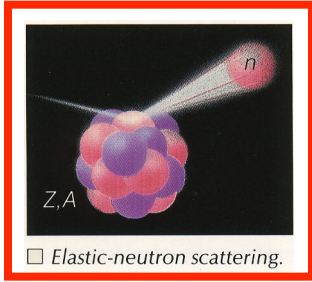Electrical current out

Photoelectrode

Figure 7.4 Schematic of a scintillation counter. An incident gamma ray on the scintillation crystal of NaI causes the crystal to emit a photon, which then causes the photoelectrode to emit electrons. The number of electrons is multiplied as each strikes a series of electrodes, finally being collected by an anode where the consequent current is proportional to the energy of the incident gamma ray.
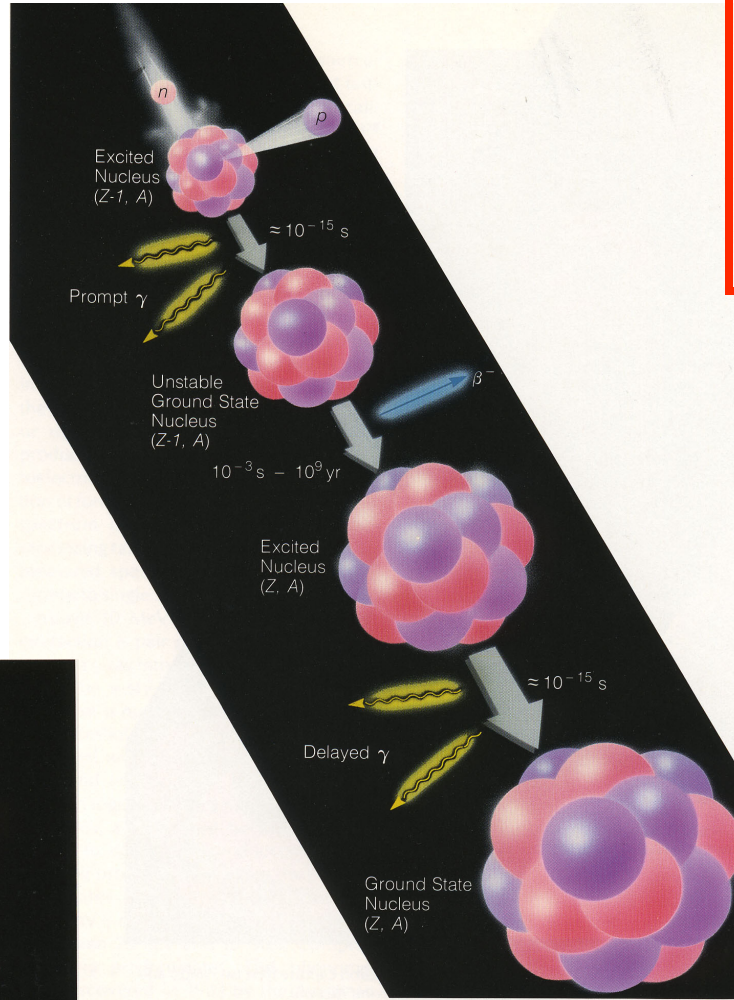

Mudcake

Long spacing detector

Short spacing detector
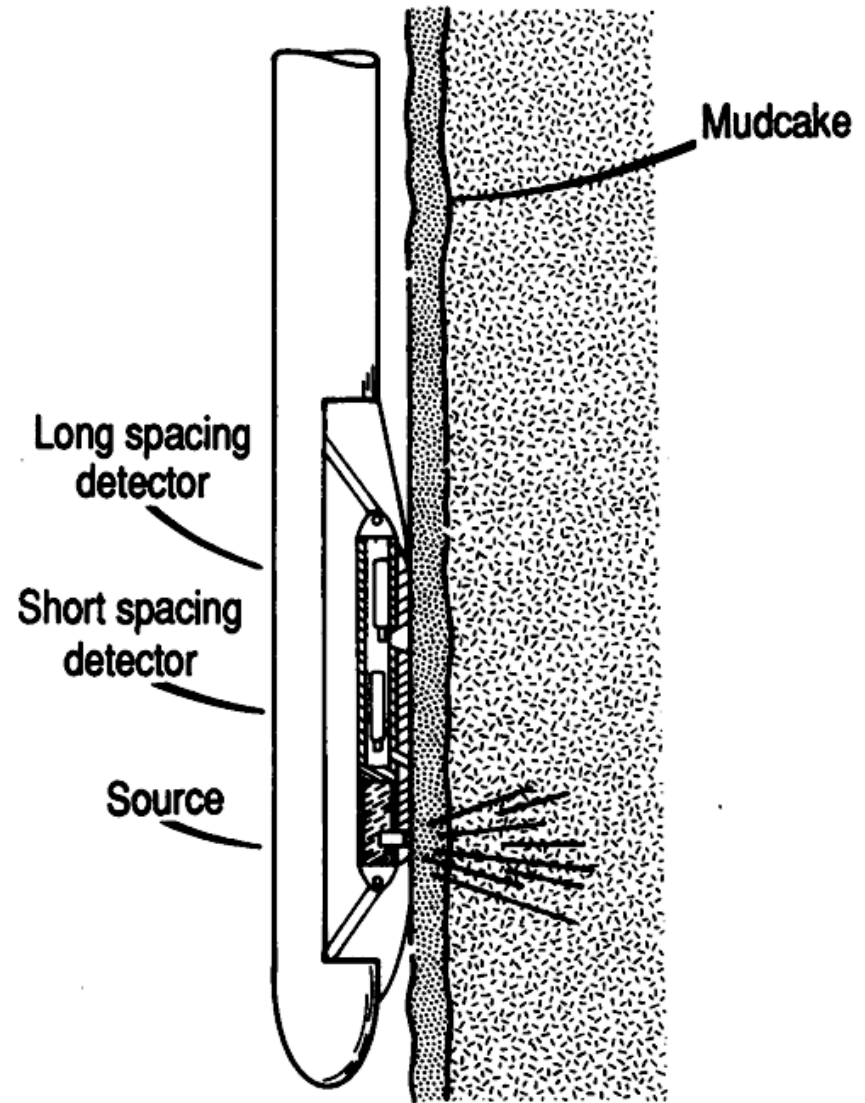
Source

Electron density index $\rho_e \equiv 2\dfrac{Z}{A}\rho_b$

Fast/slow *n*

Elastic-neutron scattering.

Neutron porosity

Fast *n*

Inelastic-neutron scattering.

Fast *n*

Excited Nucleus (Z-1, A)

$\approx 10^{-15}$ s

Prompt γ

Unstable Ground State Nucleus (Z-1, A)

10^{-3} s – 10^{9} yr

β⁻

Excited Nucleus (Z, A)

$\approx 10^{-15}$ s

Delayed γ

Ground State Nucleus (Z, A)

Fast-neutron particle reaction.

Slow *n*

Capture spectroscopy

Excited Nucleus (Z, A+1)

$\approx 10^{-15}$ s

Prompt γ

Unstable Ground State Nucleus (Z, A+1)

10^{-3} s – 10^{9} yr

β∓

Excited Nucleus (Z±1, A+1)

$\approx 10^{-15}$ s

Delayed γ

Ground State Nucleus (Z±1, A+1)

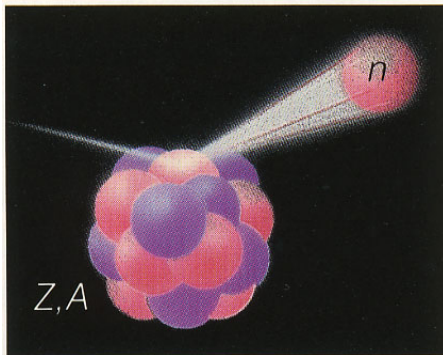Thermal neutron capture (first two steps) and activation (second step on).

Fast *n* sources:
- ^{241}Am-^{9}Be (4.35 MeV)
- Accelerator (14MeV)
Thermal *n* energy = 0.025eV

Elastic-neutron scattering.

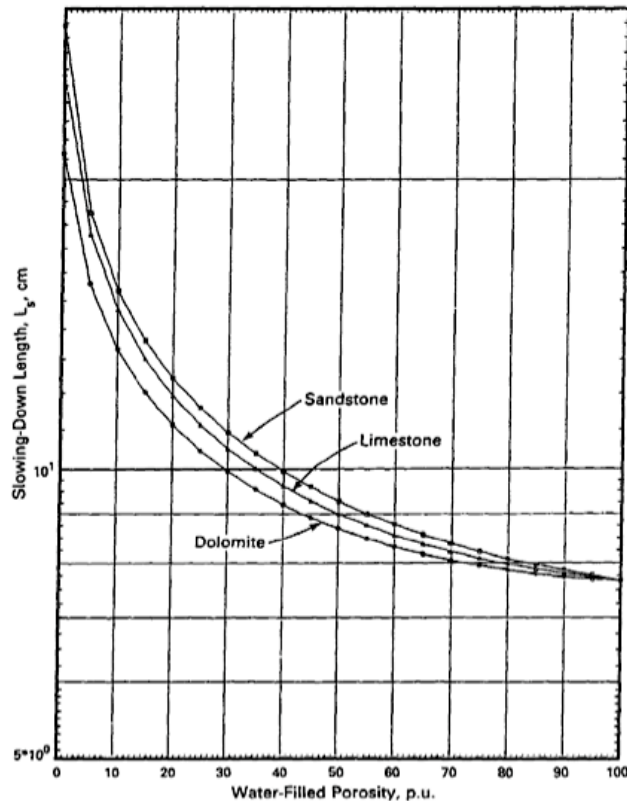
Figure 1 The slowing-down length of three common rock types as a function of porosity. From Ellis (36).

- Neutrons lose most energy bouncing off H nuclei
- Slowing-down length for high-energy neutrons to reach epithermal energy (0.1-10 eV) depends on water-filled porosity
- Measurement: flux of thermal-epithermal scattered neutrons

Fig. 5. Neutron and density log estimates of porosity (ϕ_{th}, thermal neutrons; ϕ_{epi}, epithermal neutrons; ϕ_d, density). Agreement between the three is seen in a sandstone layer, which contains no clay minerals. In the shale zones above and below, the neutron estimates exceed the density estimate because of the high H concentration associated with the clay minerals. [Adapted from (11)]
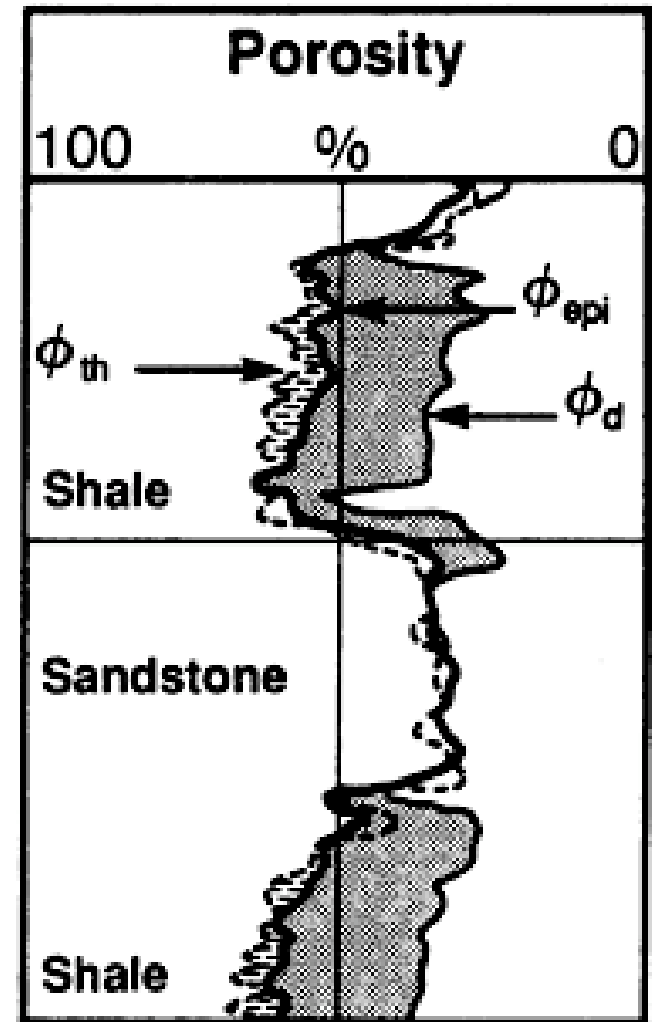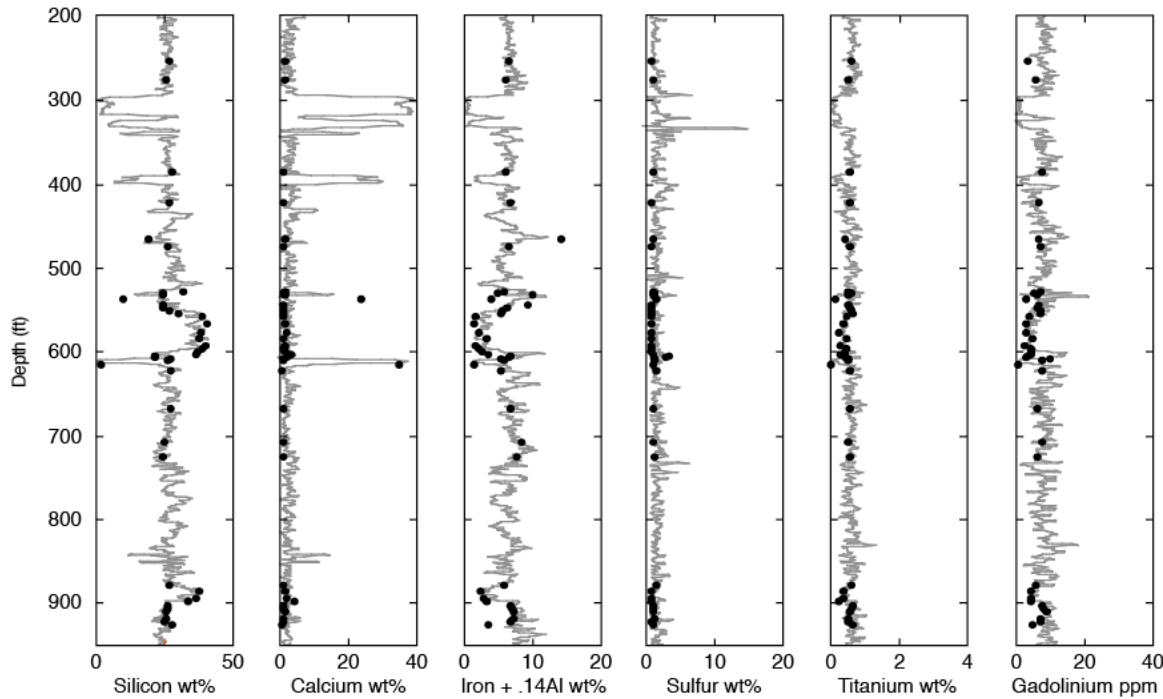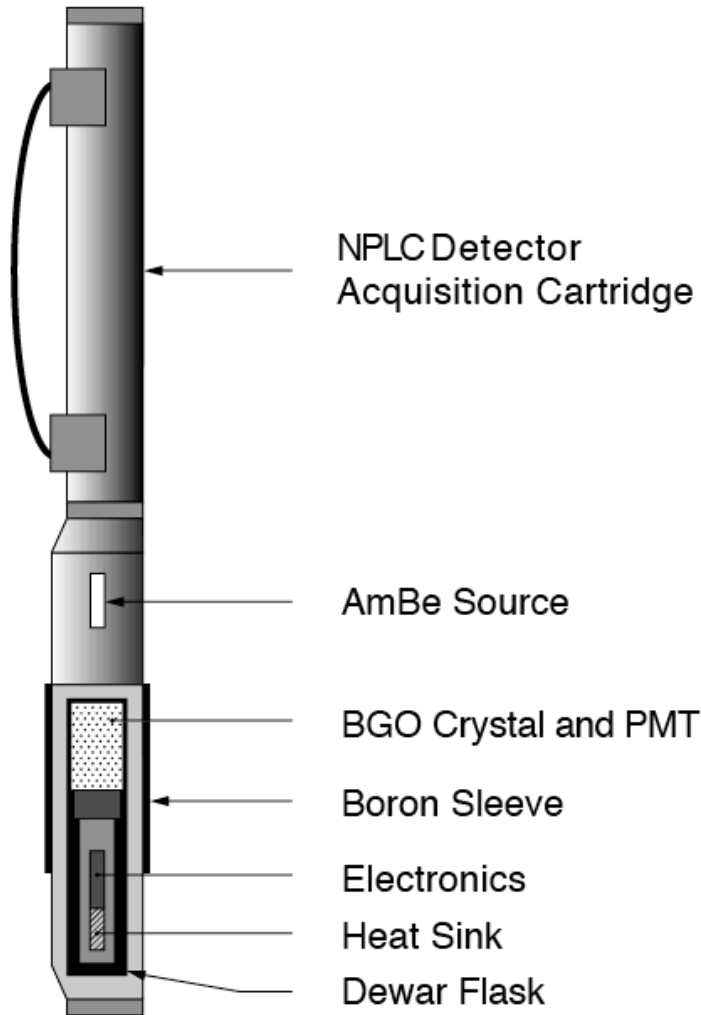
Thermal *n* capture spectroscopy

Excited Nucleus (Z, A + 1)

≈ 10^{-15} s

Prompt γ
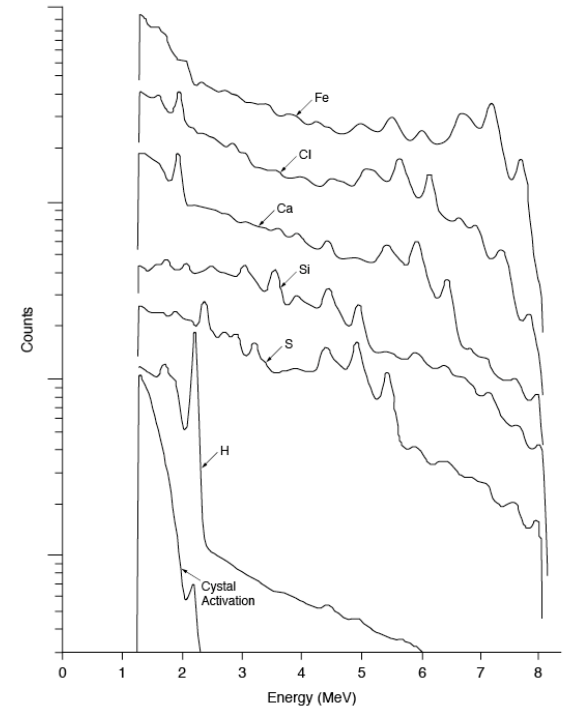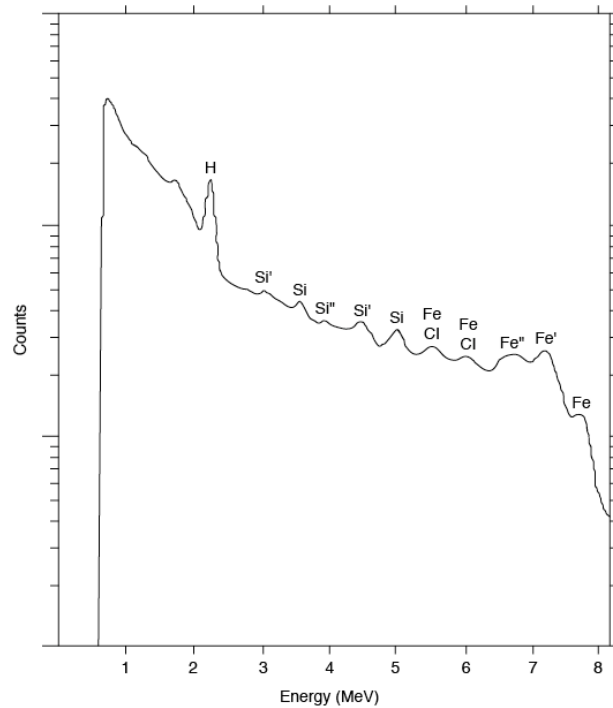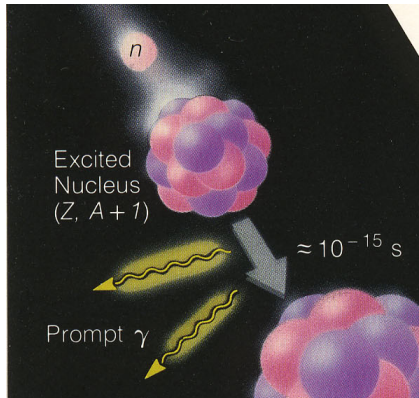
$$\text{Measured gamma-ray spectrum} = \sum \text{Elemental yield} \times \text{Element gamma-ray spectrum}$$

Detection depends on
- Thermal *n* absorption cross-section
- Character of gamma ray spectrum
- Elemental abundance

NPLC Detector Acquisition Cartridge

AmBe Source

BGO Crystal and PMT

Boron Sleeve

Electronics

Heat Sink

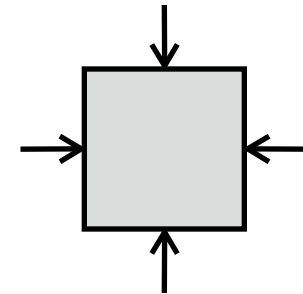Dewar Flask

• = Core plug analysis

Elemental Capture Spectroscopy (ECS) measures elemental concentrations of Si, Ca, S, Fe, Ti, and Gd

- Nuclear Logs
- Sonic
  - Monopole
  - Dipole
- Electrical / magnetic
- Imaging
- Vertical seismic profile (VSP)
- Logging While Drilling
- Examples

$$V_P = \sqrt{\frac{K + \frac{4}{3}\mu}{\rho}} \qquad V_S = \sqrt{\frac{\mu}{\rho}}$$

Compressional (P) waves
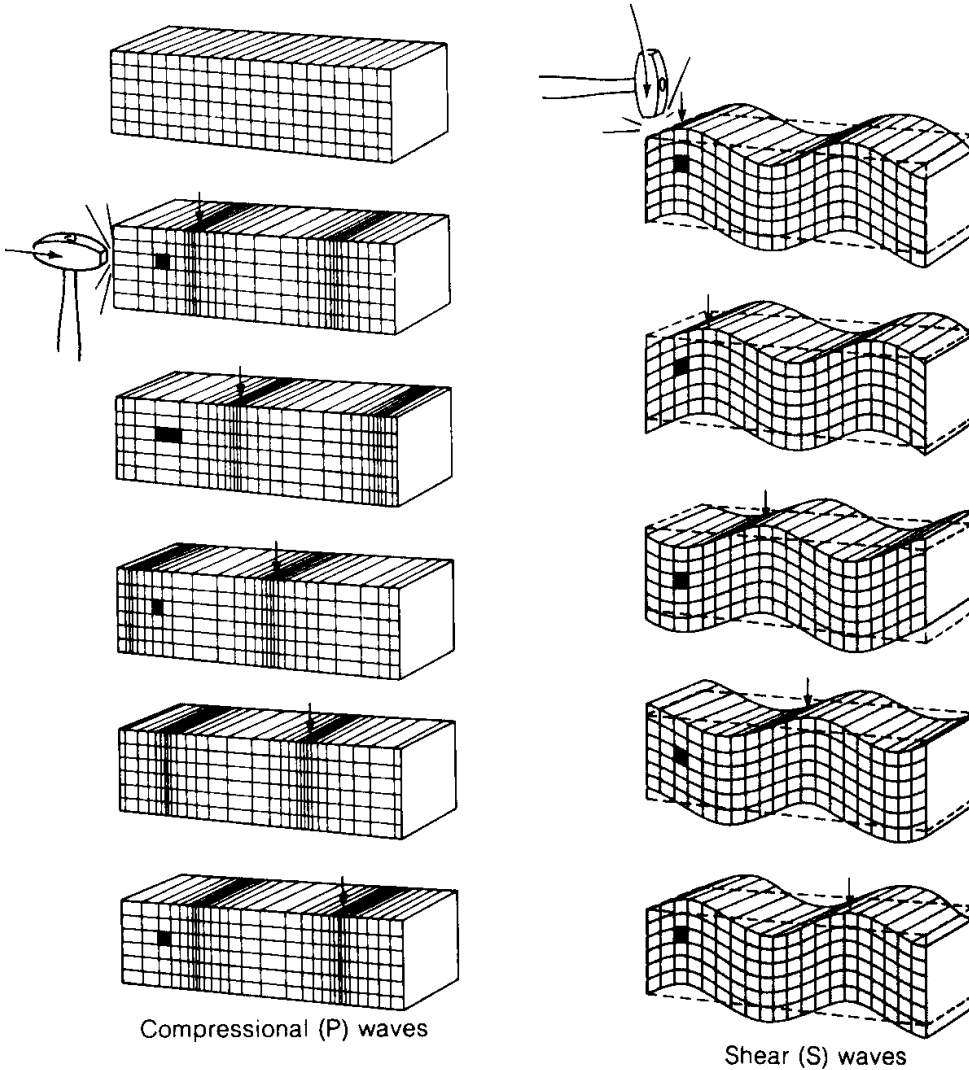
Shear (S) waves

Bulk modulus K relates compressional stress and strain
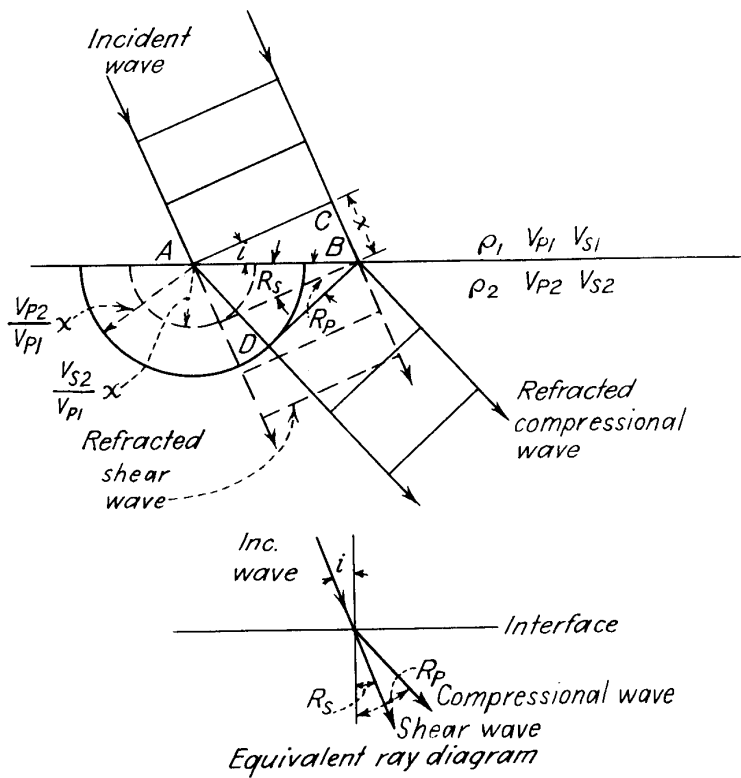
Shear modulus μ relates shear stress and strain

FIGURE 2-14

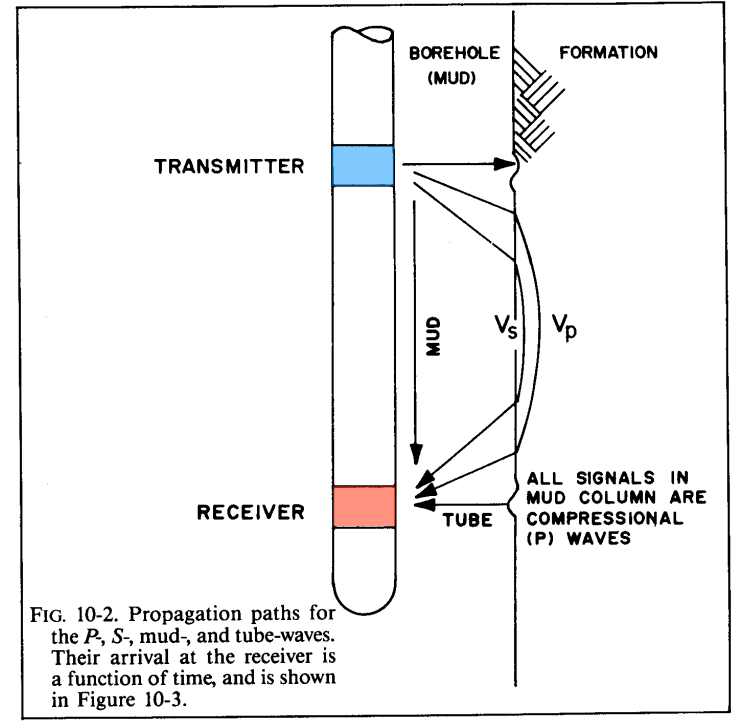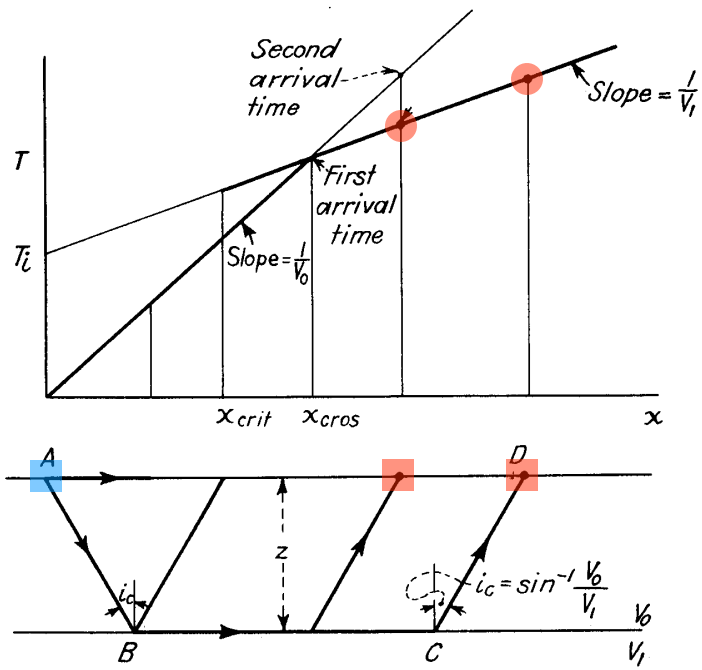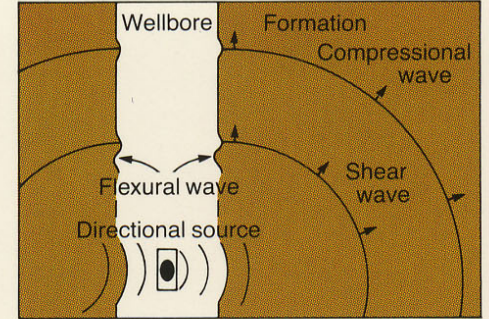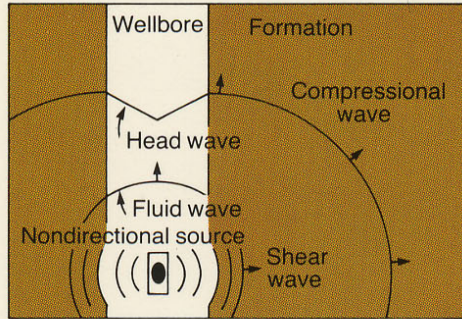Refraction of plane compressional wave across interface.

Incident wave

ρ_1 V_{P1} V_{S1}
ρ_2 V_{P2} V_{S2}

$\frac{V_{P2}}{V_{P1}} x$

$\frac{V_{S2}}{V_{P1}} x$

Refracted shear wave

Refracted compressional wave

Inc. wave

Interface

R_P
Compressional wave

R_S
Shear wave

Equivalent ray diagram

BOREHOLE (MUD)   FORMATION

TRANSMITTER

MUD V_s V_p

RECEIVER   TUBE

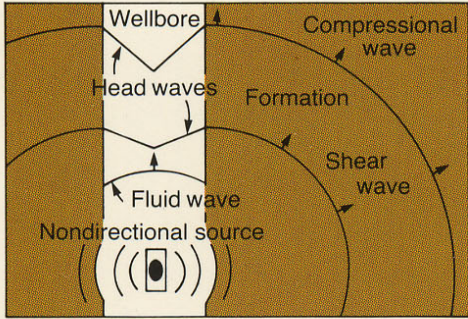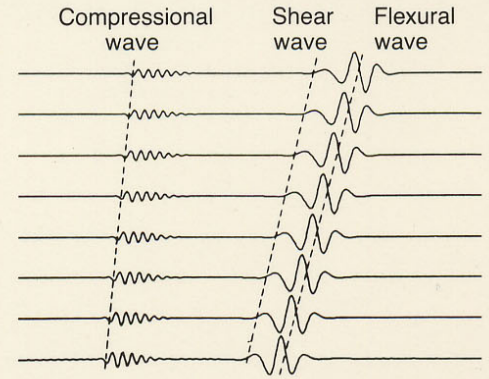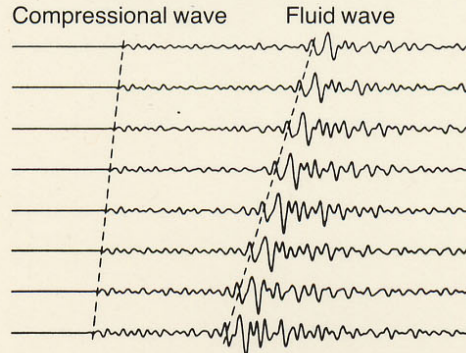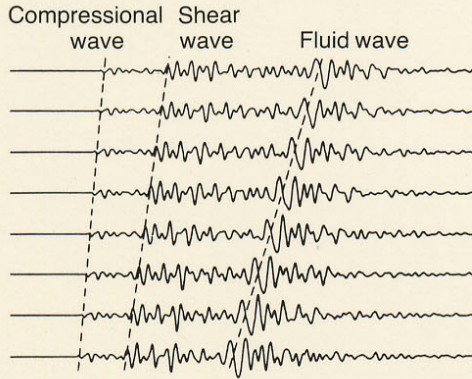ALL SIGNALS IN MUD COLUMN ARE COMPRESSIONAL (P) WAVES

FIG. 10-2. Propagation paths for the P-, S-, mud-, and tube-waves. Their arrival at the receiver is a function of time, and is shown in Figure 10-3.

Second arrival time

Slope = $\frac{1}{V_1}$

First arrival time

Slope = $\frac{1}{V_0}$

T

T_i

x_{crit} x_{cros} x

A D

z

i_c $i_c = sin^{-1} \frac{V_0}{V_1}$

B C $\frac{V_0}{V_1}$

Sound Wave Propagation

Sonic Waveforms

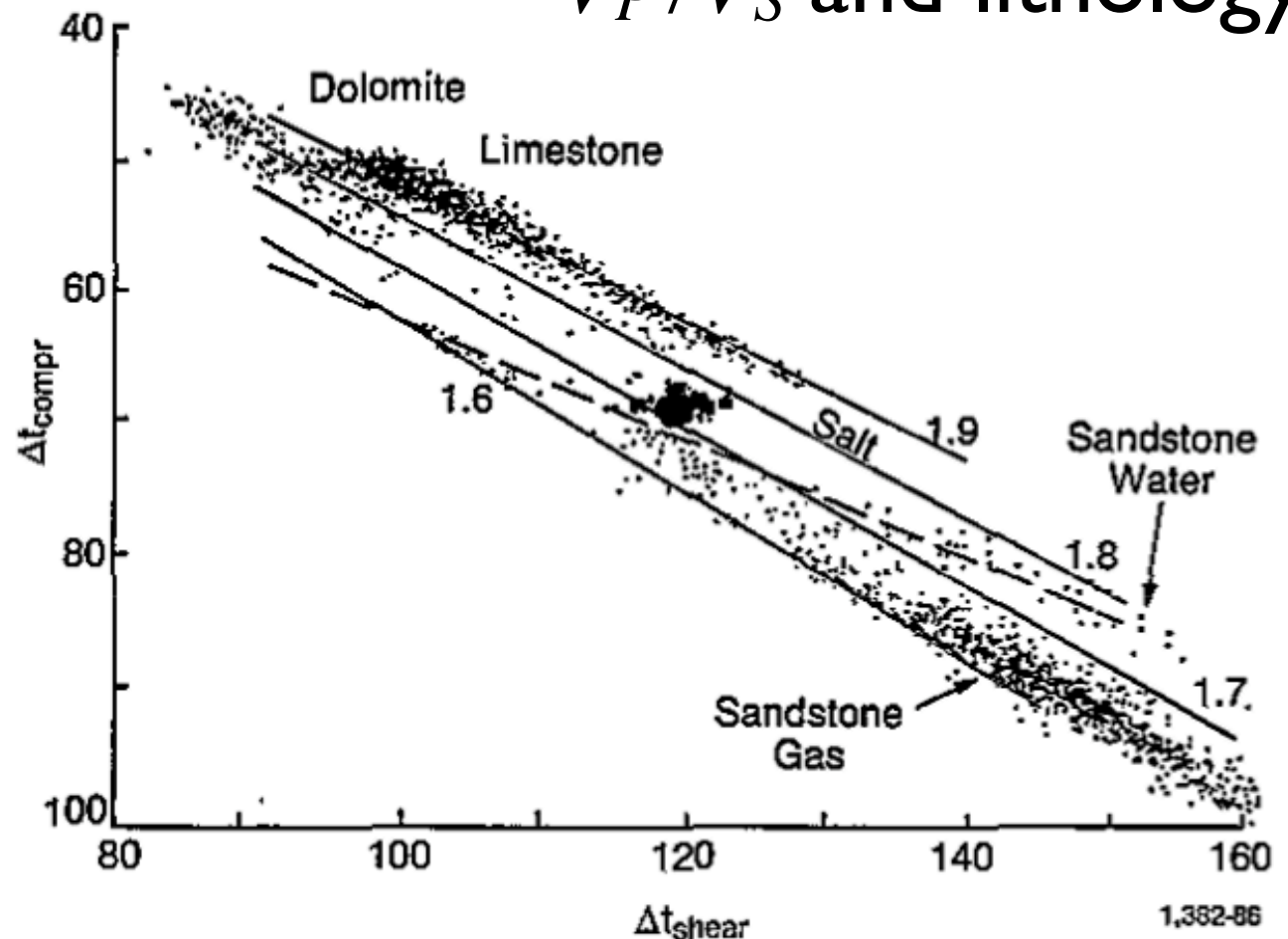"Fast" formation   "Slow" formation   "Slow" formation

Wyllie's time-average
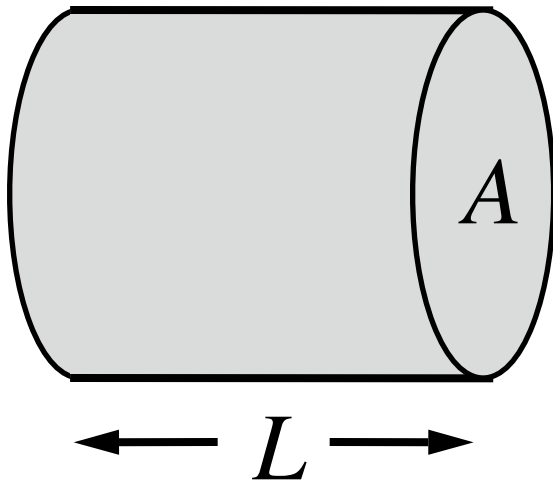## Slowness $u = 1/V_P$

$$u = (1 - \phi)u_g + \phi u_f$$

V_P/V_S and lithology

- Nuclear Logs
- Sonic
- Electrical / magnetic
  - Resistivity
    - Electrode devices
    - Induction
  - Magnetic susceptibility
- Imaging
- Vertical seismic profile (VSP)
- Logging While Drilling
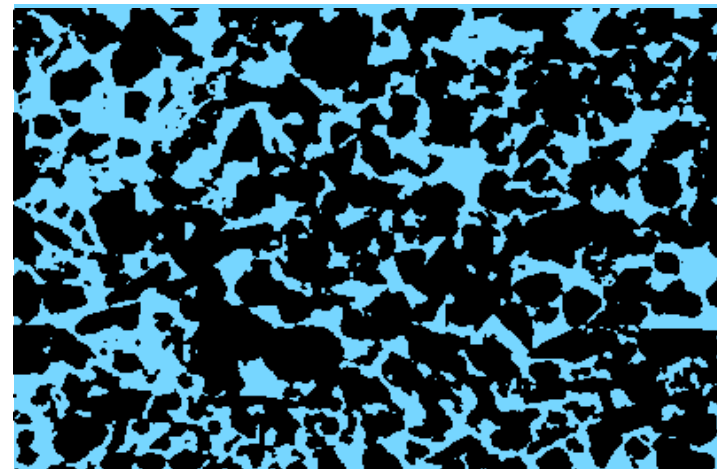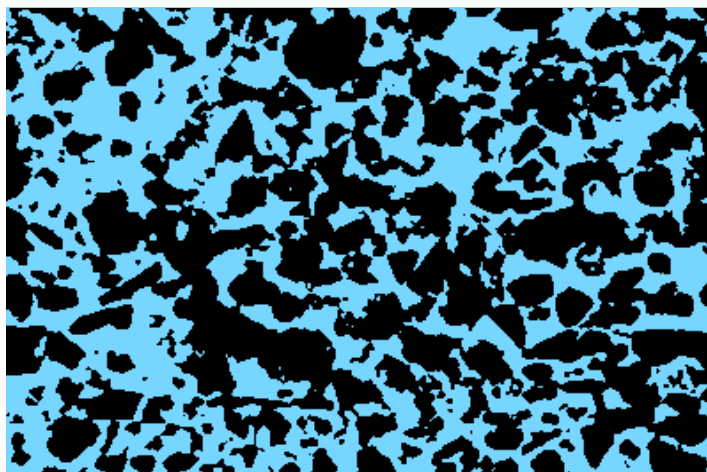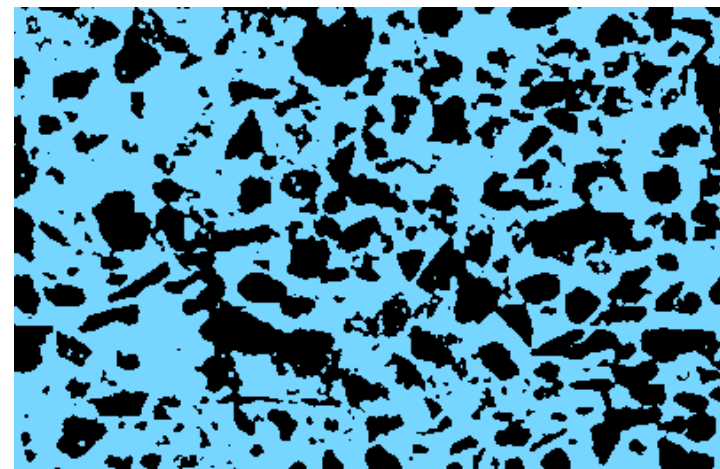- Examples

Electrical properties

Ohm's law

$$V = IR^*$$

Resistance R^*
Resistivity R

$$R^* = R\frac{L}{A}$$
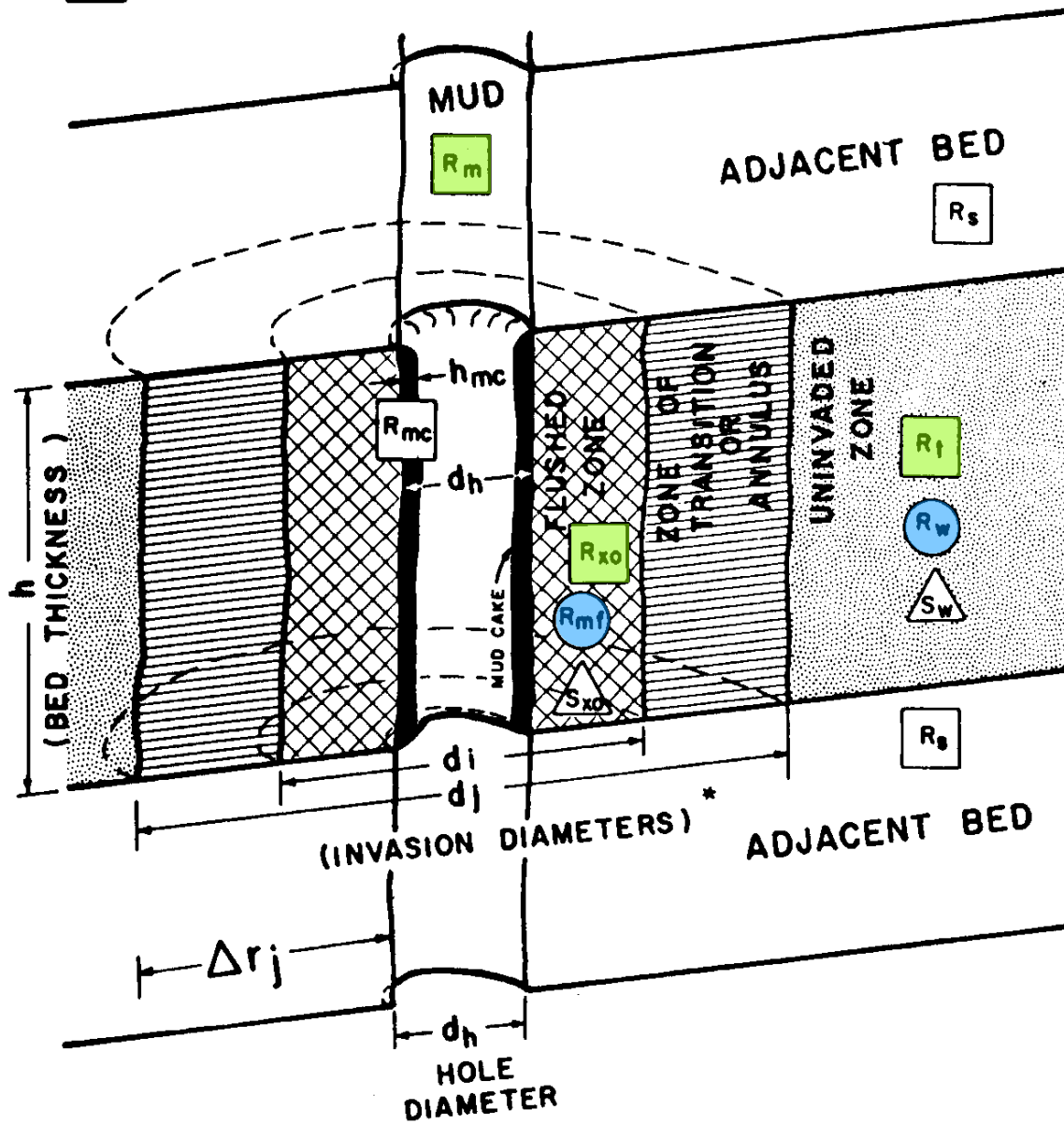
Units of resistivity are $\Omega \cdot m$ (ohm·m)

Resistivity

Water

Porosity

Resistivity of the zone

Resistivity of the Water in the zone

Water Saturation in the zone.

MUD

R_m

ADJACENT BED

R_s

R_{mc}

h_{mc}

d_h

MUD CAKE

FLUSHED ZONE

ZONE OF TRANSITION OR ANNULUS

UNINVADED ZONE

R_t

R_w

R_{xo}

R_{mf}

S_{xo}

S_w

(BED THICKNESS) h

R_s

d_i

d_j

(INVASION DIAMETERS) *

ADJACENT BED

Δr_j

d_h

HOLE DIAMETER

Water wet sand

Oil wet sand

(a)

(d)

(b)

(e)

(c)

(f)

☐ Water   ■ Oil

1927

$$R_a = \frac{4\pi \Delta V}{I} r$$

Meter

Generator

B

N

M

A

O

r

1,352-86
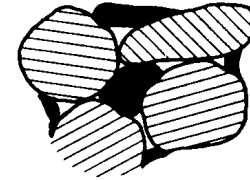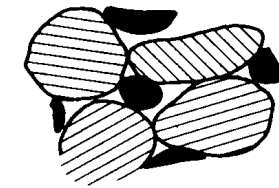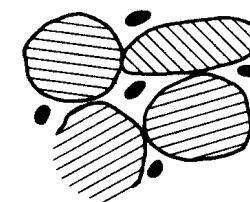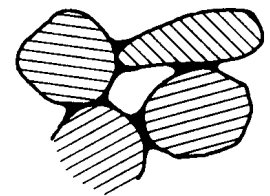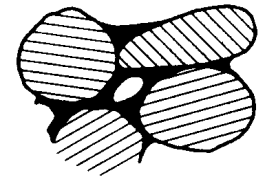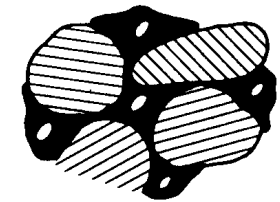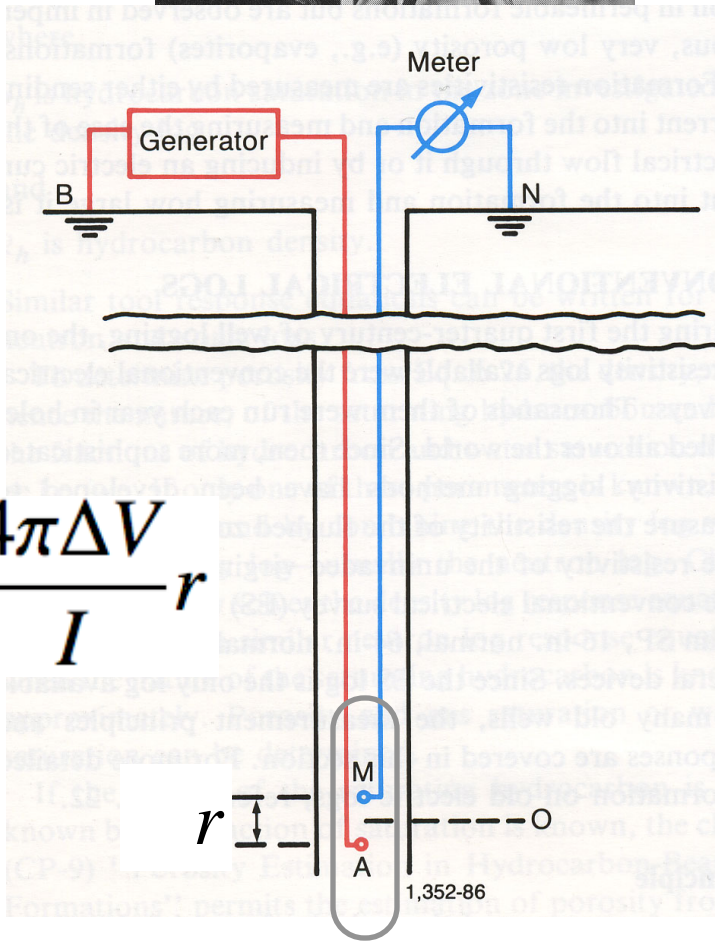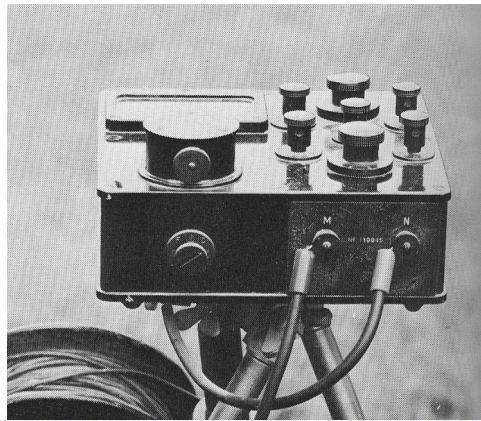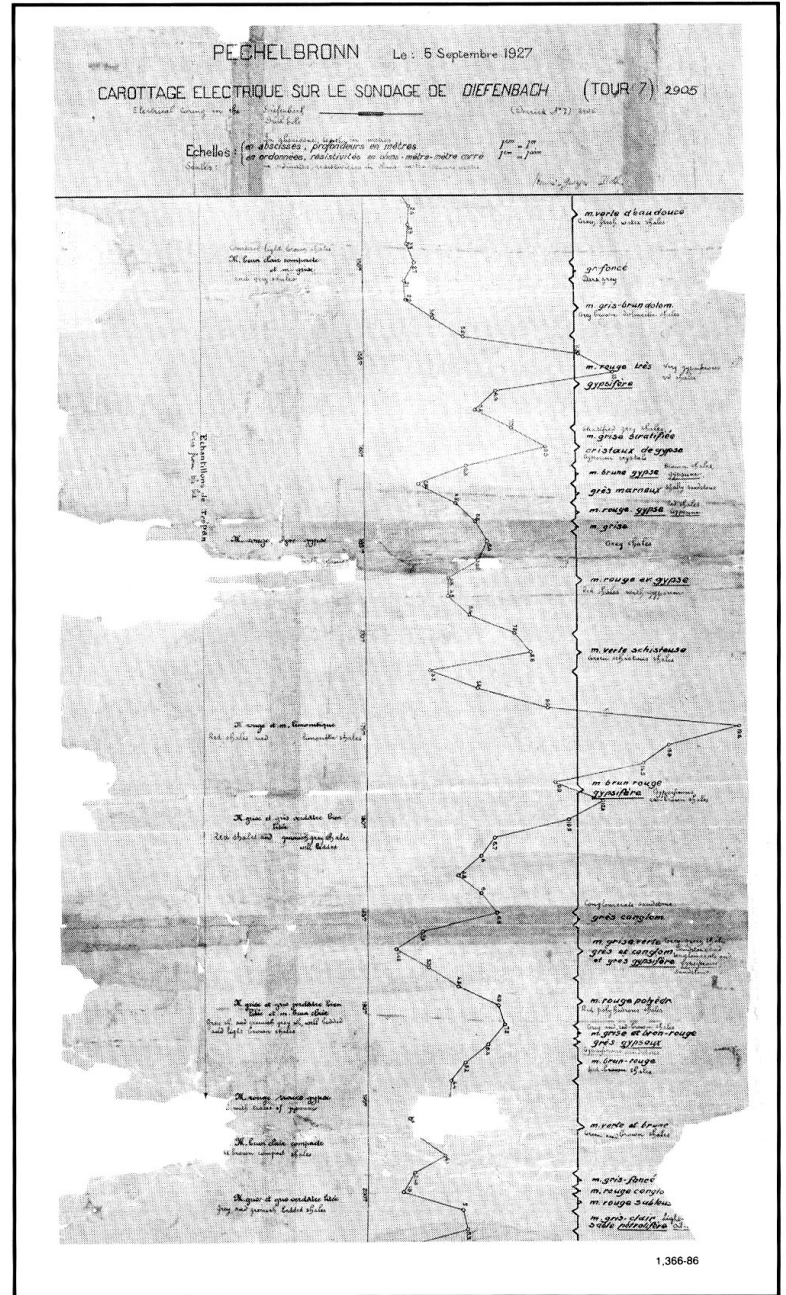
Fig. 1-1—The first log: points plotted on graph paper by Henri Doll.

LLD   LLS

A_2

A_1

M_2

M_1

A_O

i_O

M'_1

M'_2

i_a

A'_1

A'_2

1,397-86
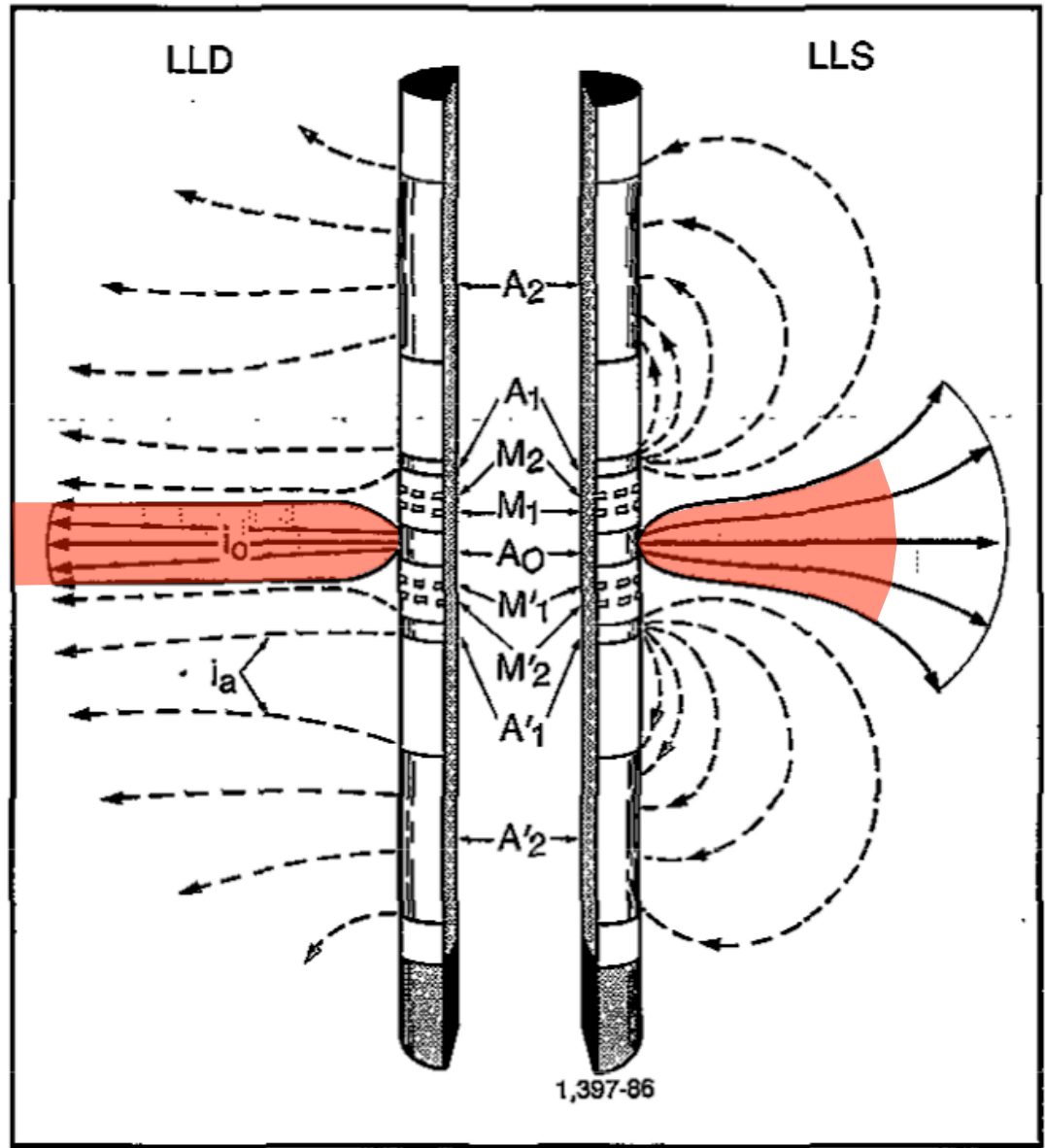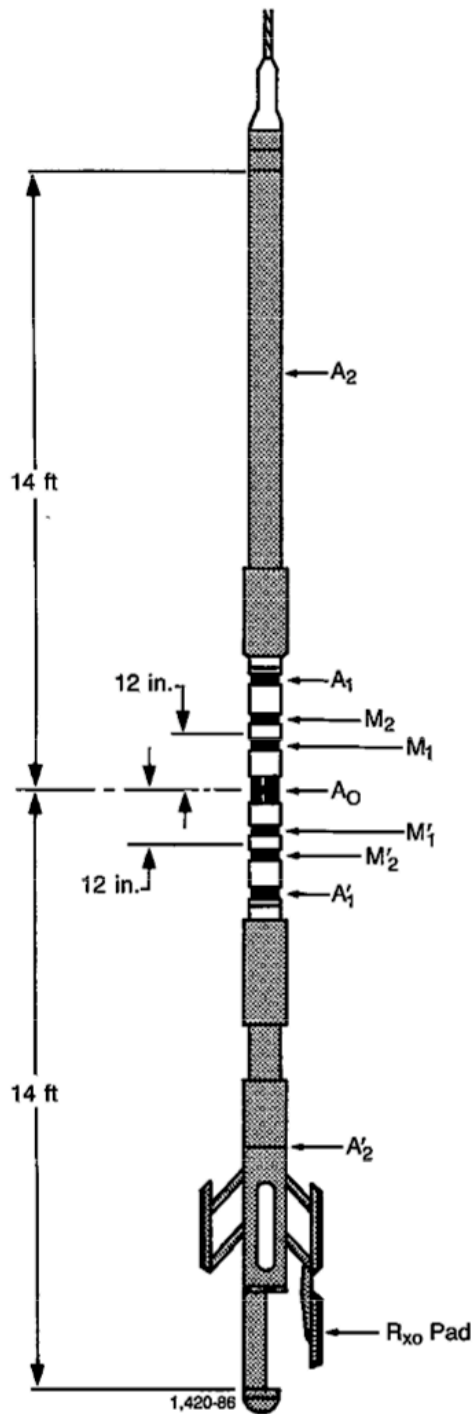
Fig. 7-13—Schematic of the Dual Laterolog.

14 ft

A_2

12 in.

A_1

M_2

M_1

A_O

M'_1

M'_2

12 in.

A'_1

14 ft

A'_2

R_{xo} Pad

1,420-86

27

FIG. 24. The basic two-coil induction sonde. Transmitter T and receiver R, separated by a distance L, are wound on an insulating mandrel. T produces an eddy current in a loop of unit cross-sectional area in the formation. This in turn induces in R an emf which is proportional to the conductivity of the material in the loop. [Adapted from H. G. Doll, *Pet. Trans. AIME* **186,** 148 (1949). Copyright 1949 SPE–AIME.]

Magnetic susceptibility χ
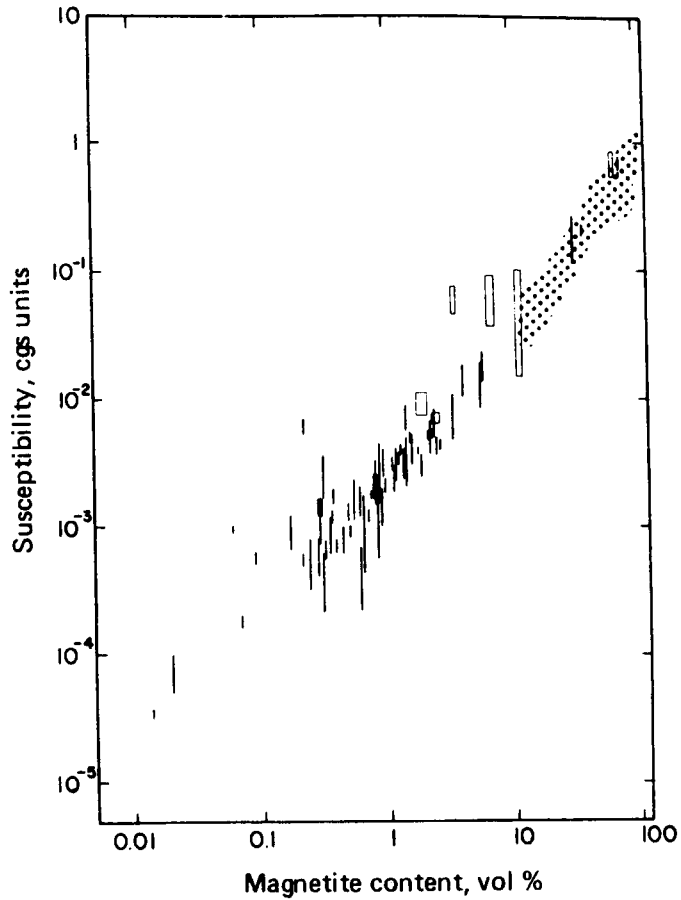
Figure 5.77 *Relation between susceptibility and magnetite content of a variety of rocks and ores compiled by Lindsley et al. (1966). Vertical lines show range due to anisotropy; box widths show variation among samples*

Susceptibility, cgs units

Magnetite content, vol %

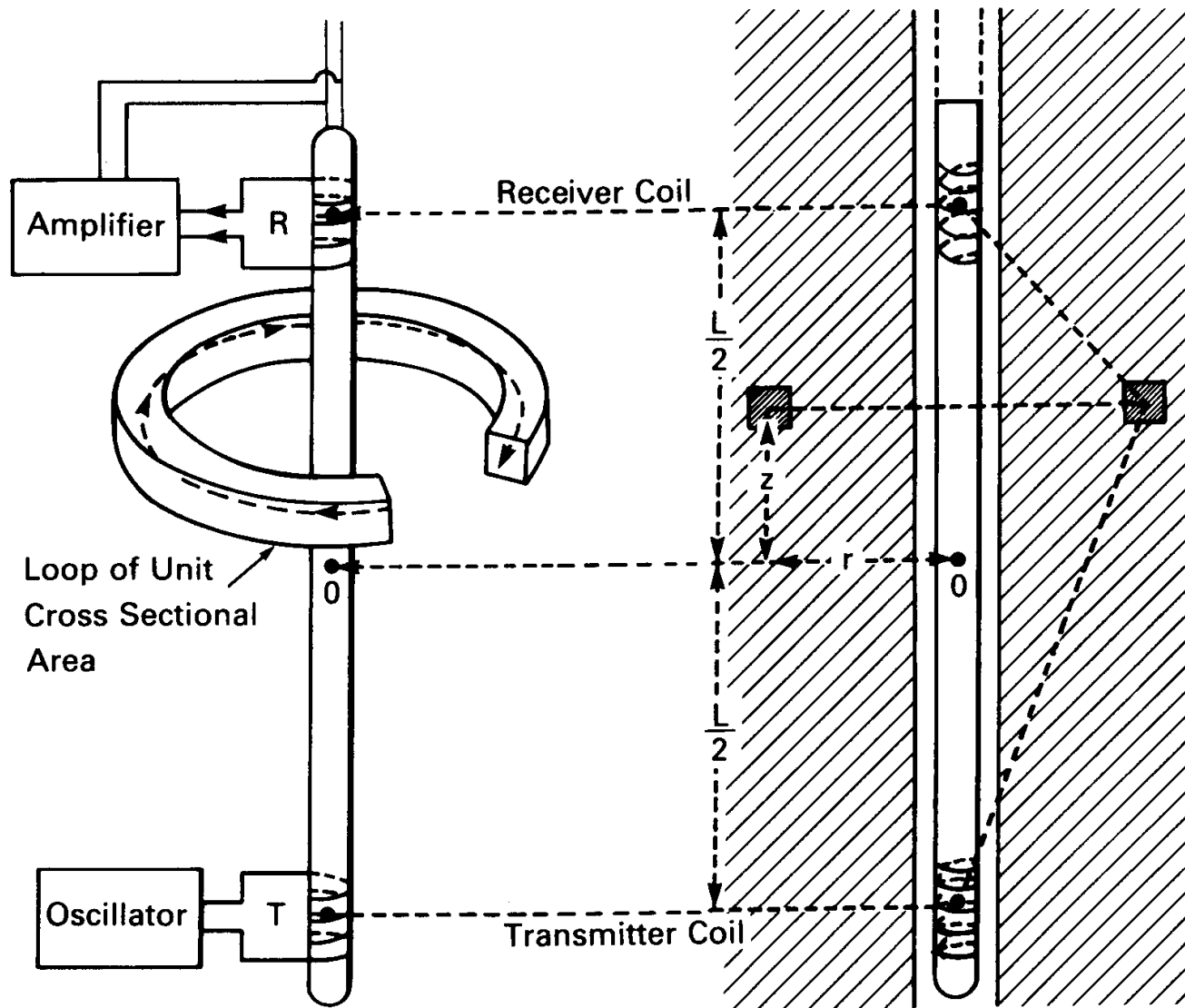Magnetic susceptibility
(core; 10⁻⁶ SI)

Natural gamma-ray activity
(core; cps)

Depth (mbsf)

Magnetic susceptibility
(arbitrary units)

Natural gamma-ray activity
(log; API)
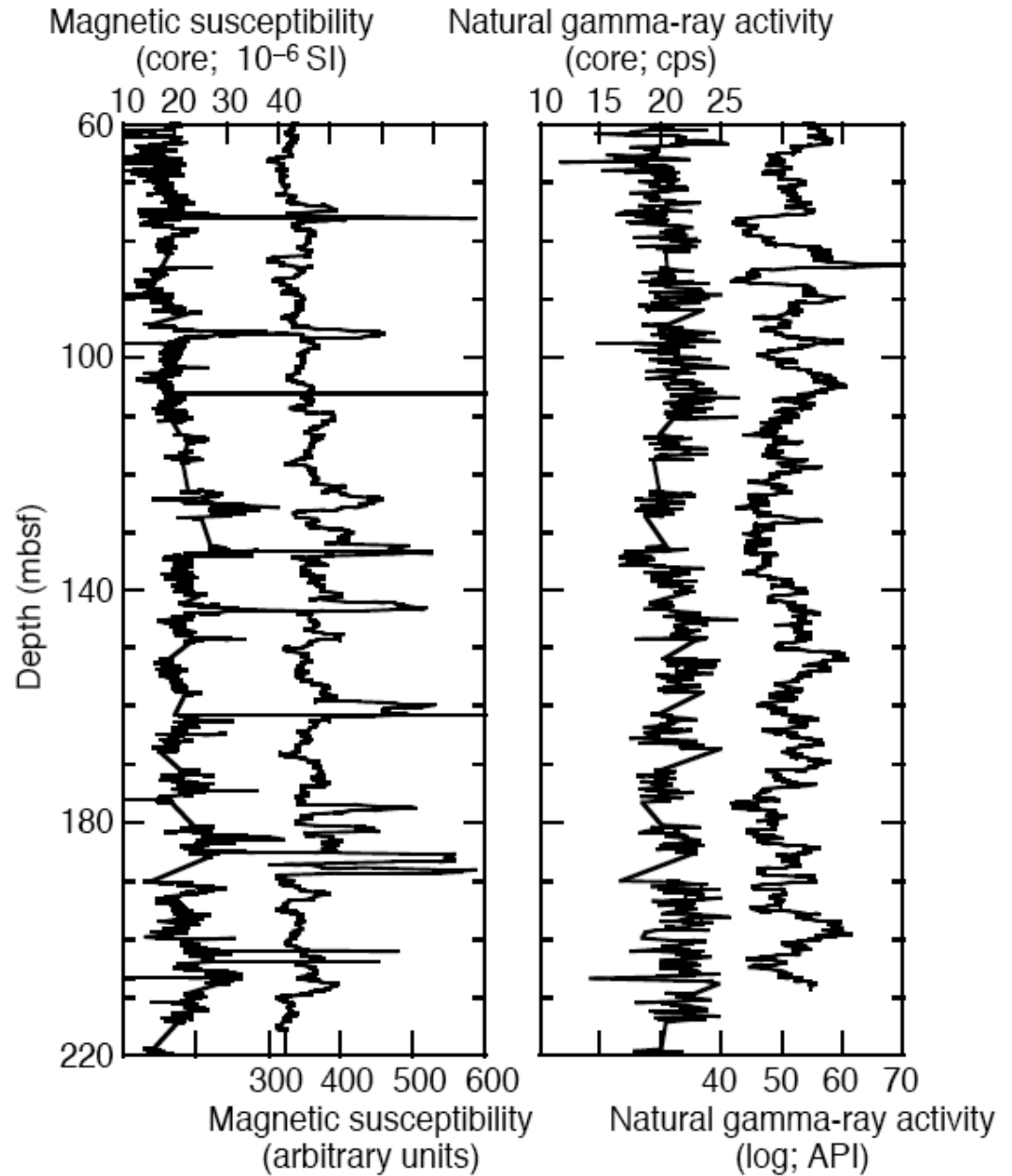
- Nuclear Logs
- Sonic
- Electrical / magnetic
- Imaging
  - Electrical
  - Acoustic
- Vertical seismic profile (VSP)
- Logging While Drilling
- Examples

Digital telemetry cartridge

Digital telemetry adapter

Tool for depth correlation

Controller cartridge

Flex joint

Isulating sub

Inclinometer

Acquisition cartridge

Four-arm sonde

192 electrodes

0.1 in = 2.54 mm

CABLE SPEED		
0	(m/h)	1000

TOOL ACCELERATION		
-1	(m/s2)	1

TOOL VELOCITY		
0	(m/h)	1000

CALIPER 1		
6	(in)	16

CALIPER 2		
6	(in)	16

FMI NORMALIZED

Orientation North
0   120   240   360

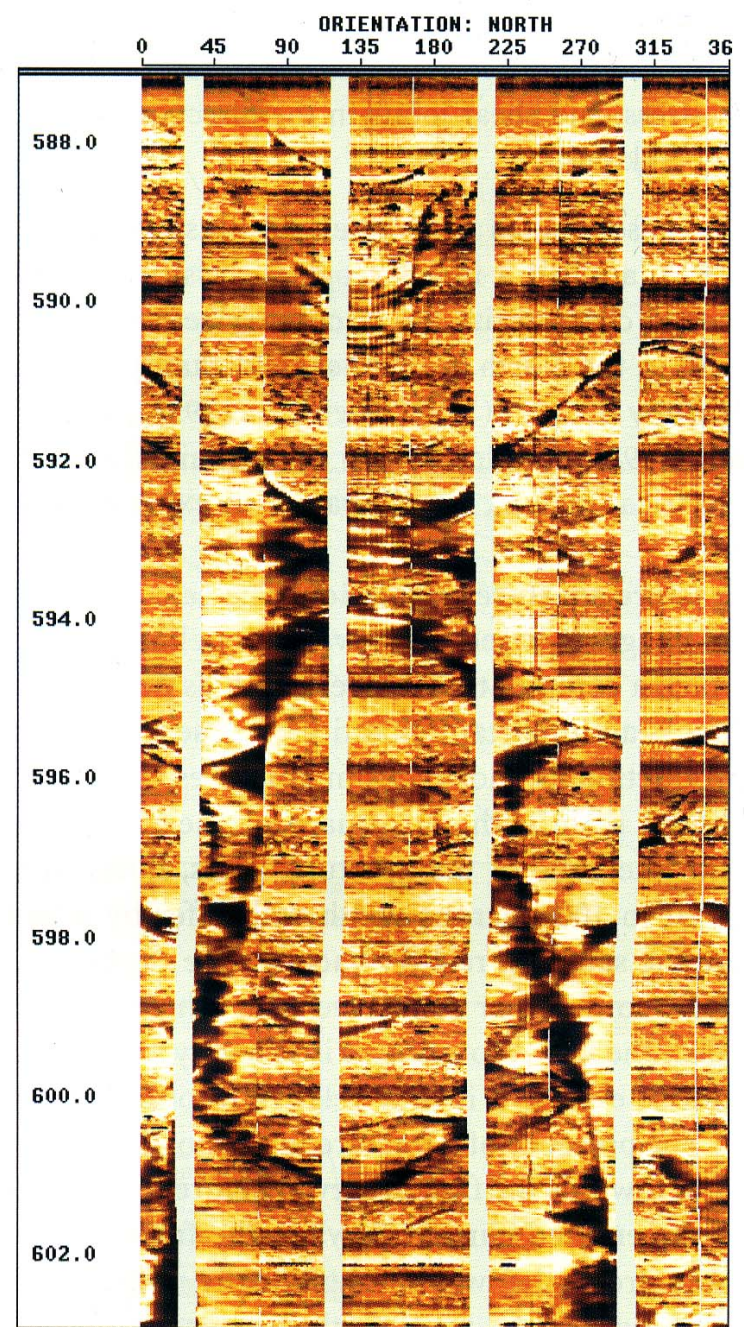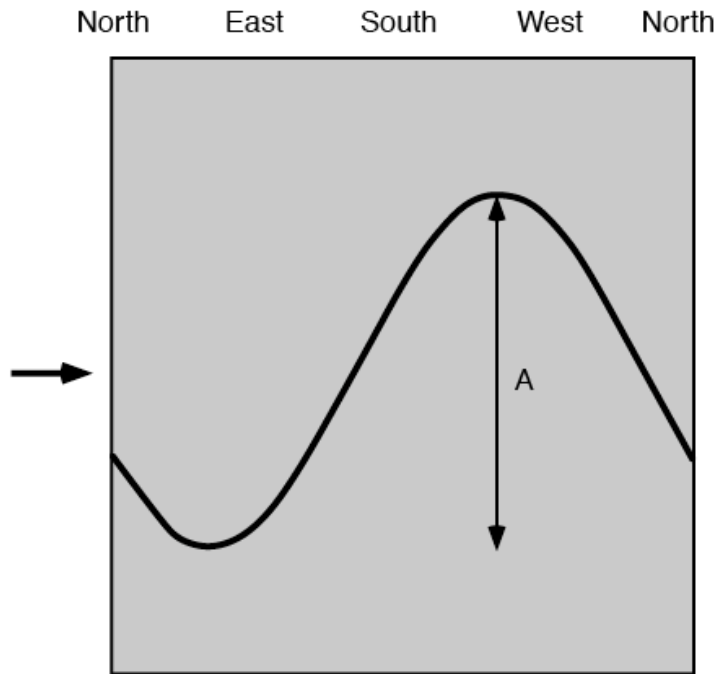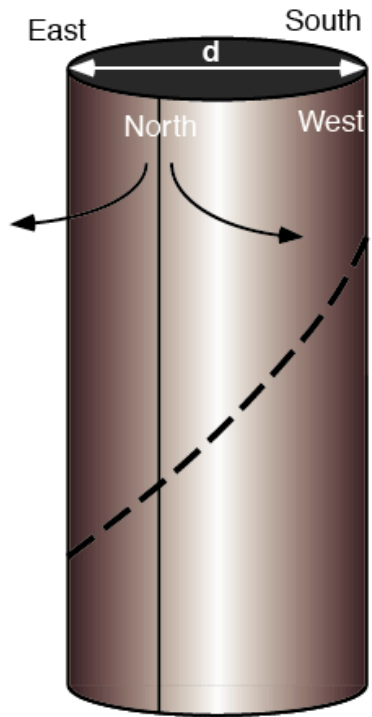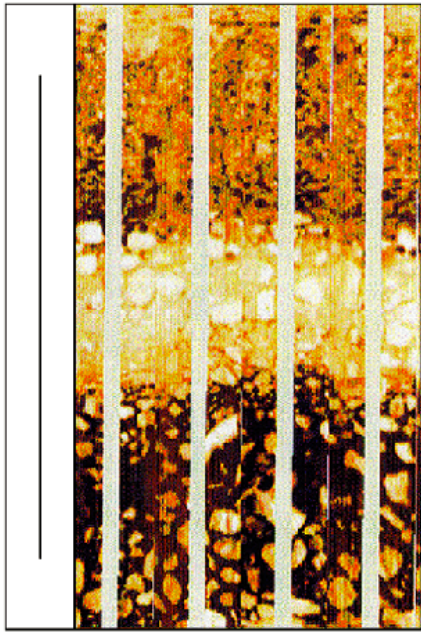Resitive   FMI Image   Conductive

m

31
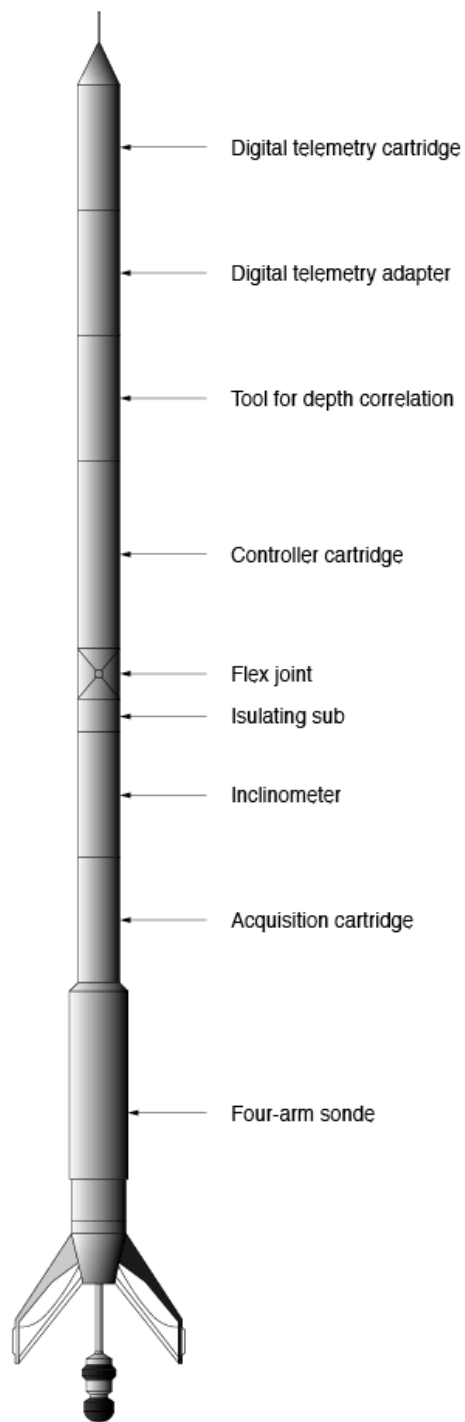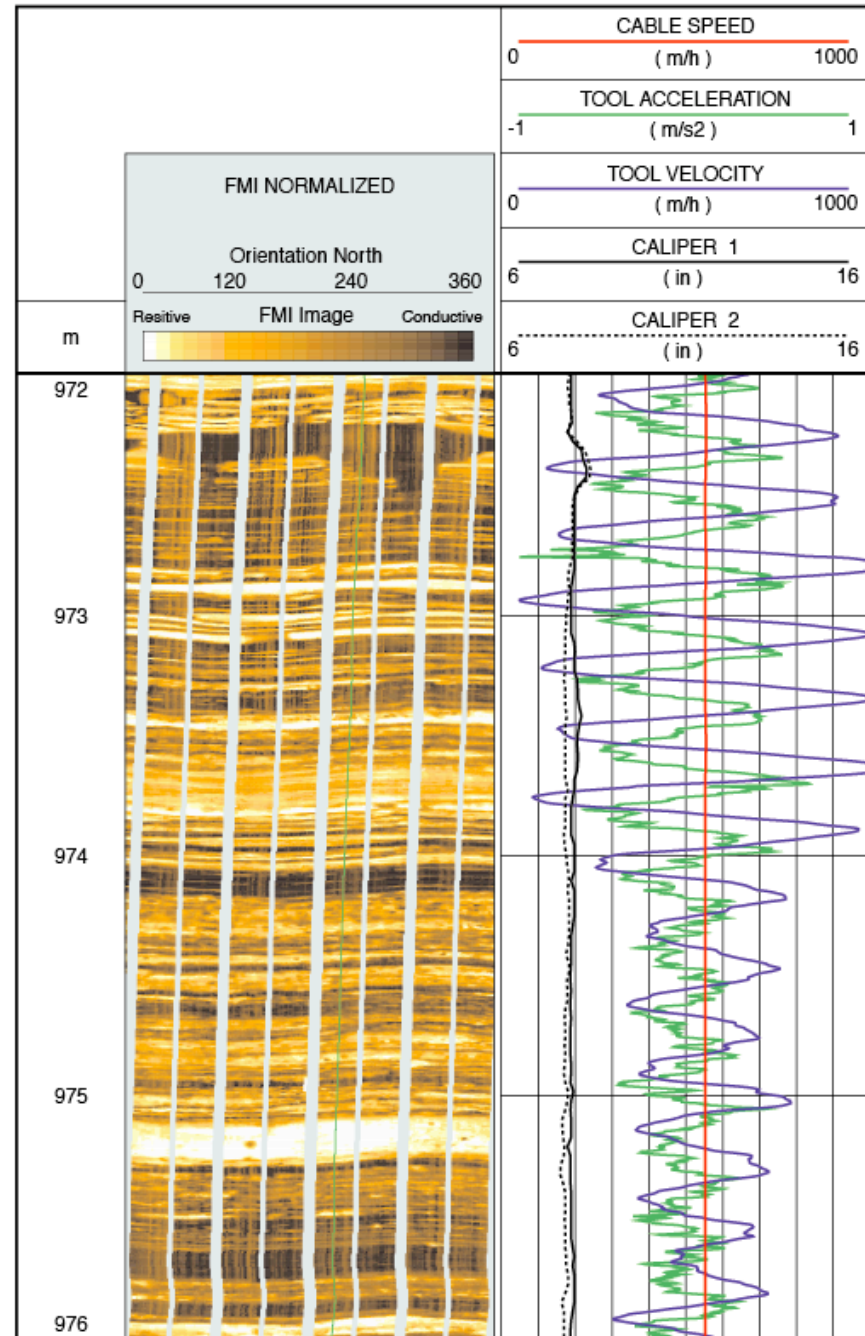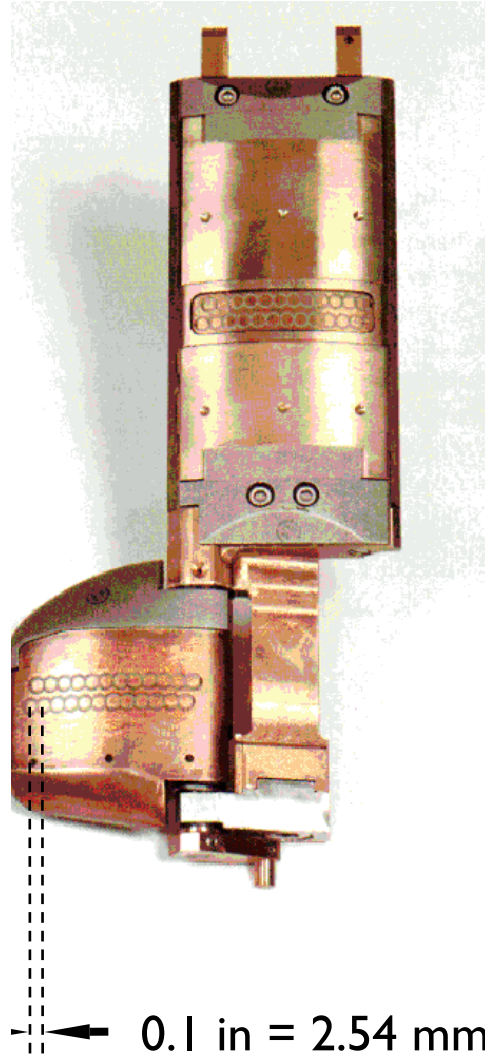
Figure 2.2.27. FMI images over a layered carbonate sequence with at least two distinct planar fracture sets, on dipping towards SSW, the other dipping steeply towards NNE.
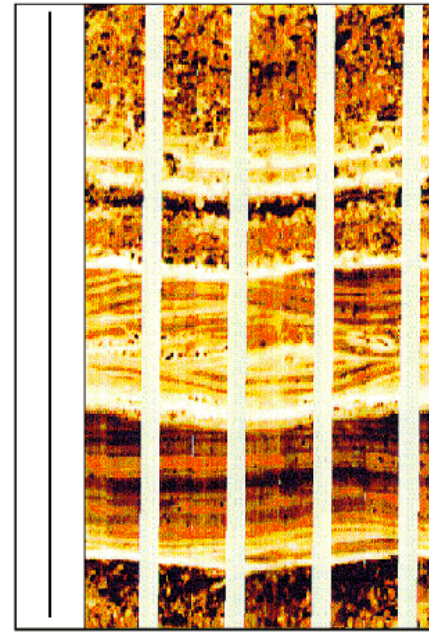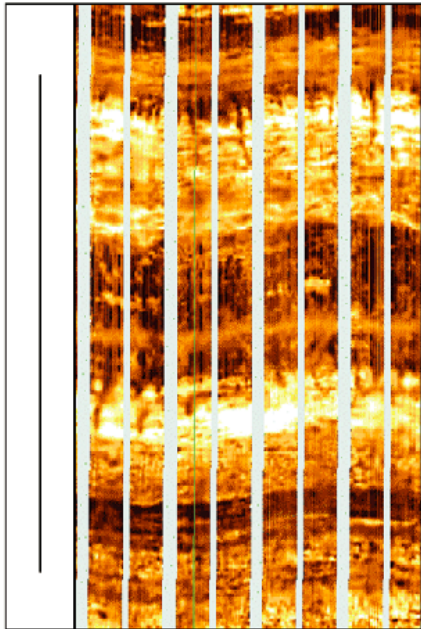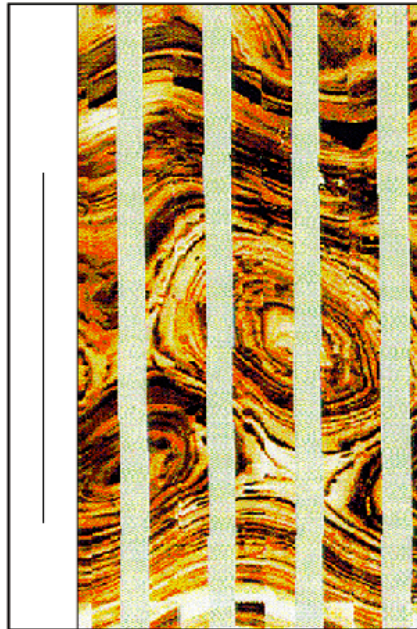
1m

Conglomerate in debris flow
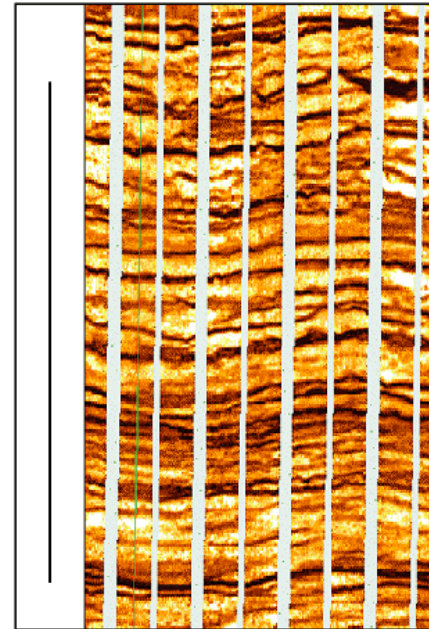
Rip-up clasts in fluvial channel

Cross-beds in tidal sandstone

Burrowing in shelf deposit

Overturned sand layers in slump

Stylolites in a limestone

are presented as a continuous record. Features are easily followed throughout any interval of the borehole.

TOOL DESCRIPTION

A schematic of the televiewer logging tool is shown in Figure 1. High frequency sound (about 2 megahertz) from an acoustic transducer, pulsed at a rate of about 2000 times a second, is used to survey the borehole walls. A flux-gate magnetometer senses the earth's magnetic field and provides orientation information in open hole. A motor rotates the transducer and flux-gate magnetometer within the tool about three times a second.

Although the transducer has a diameter of only a half-inch, the sound emitted is confined to a very narrow beam because of the high operating frequency. Pulses of sound are directed toward the borehole wall where a portion of each pulse is reflected back toward the transducer. The transducer converts the reflected sound pulses into electrical signals; these are utilized at the surface for producing the televiewer log. The combination of transducer rotation with a continuous
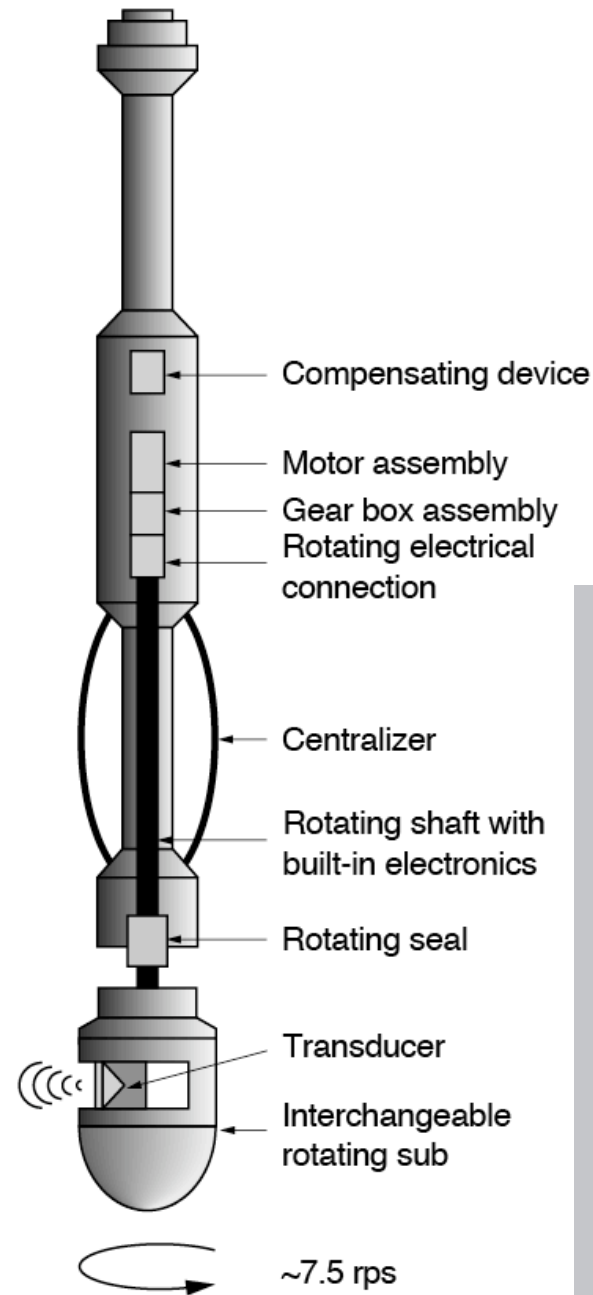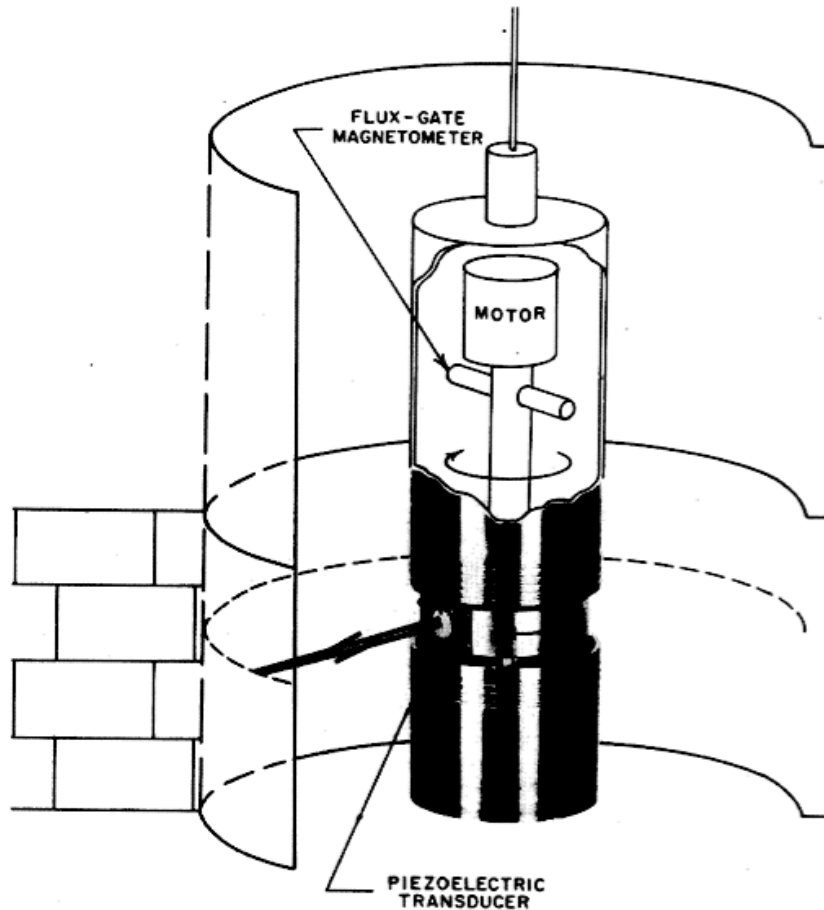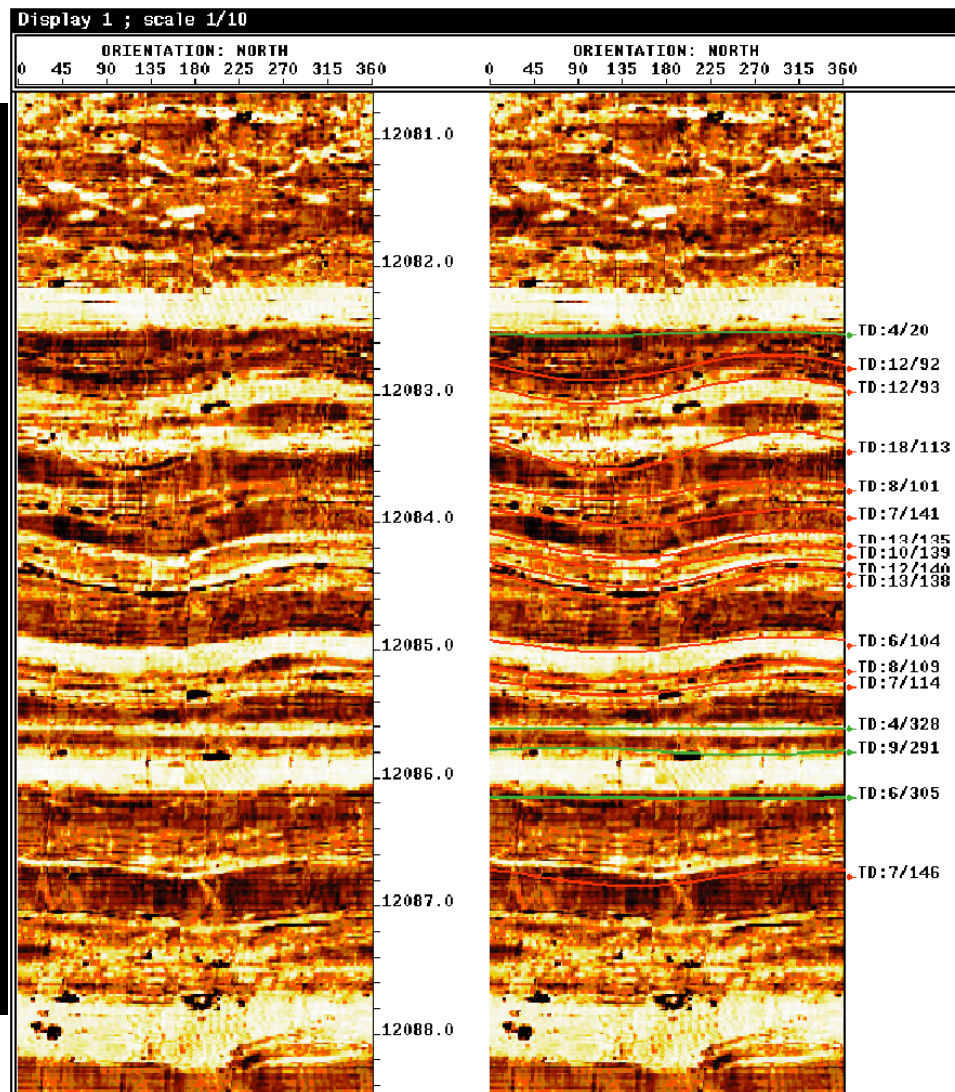

FIG. 1. Schematic layout of televiewer showing scanning acoustic transducer, magnetic north sensing magnetometer, and driving motor.
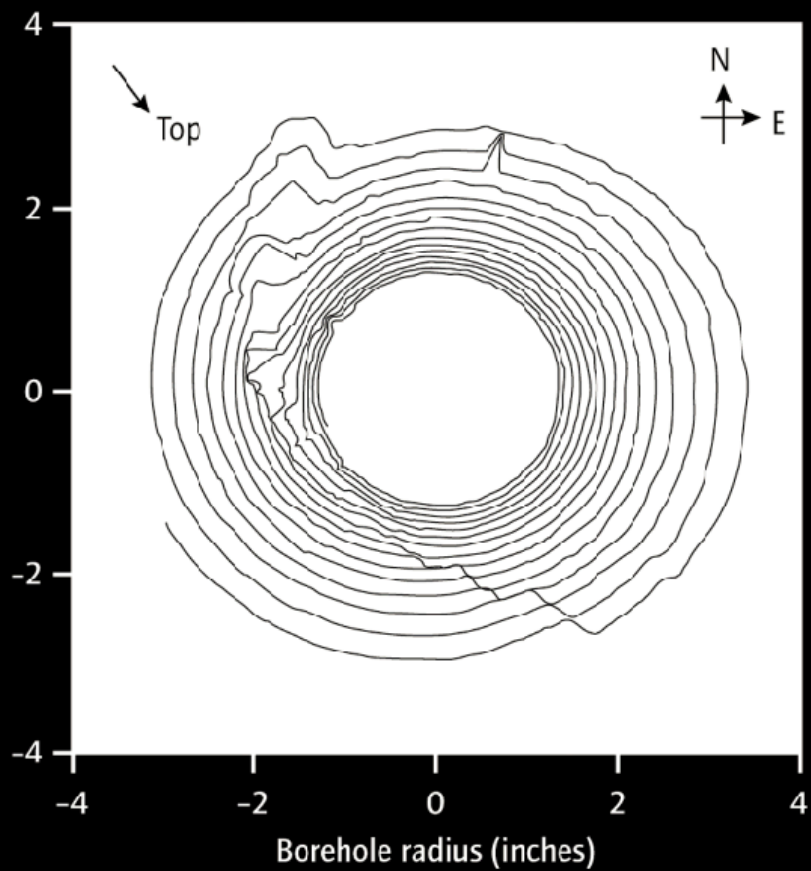
- Nuclear Logs
- Sonic
- Electrical / magnetic
- Imaging
- Vertical seismic profile (VSP)
- Logging While Drilling
- Examples
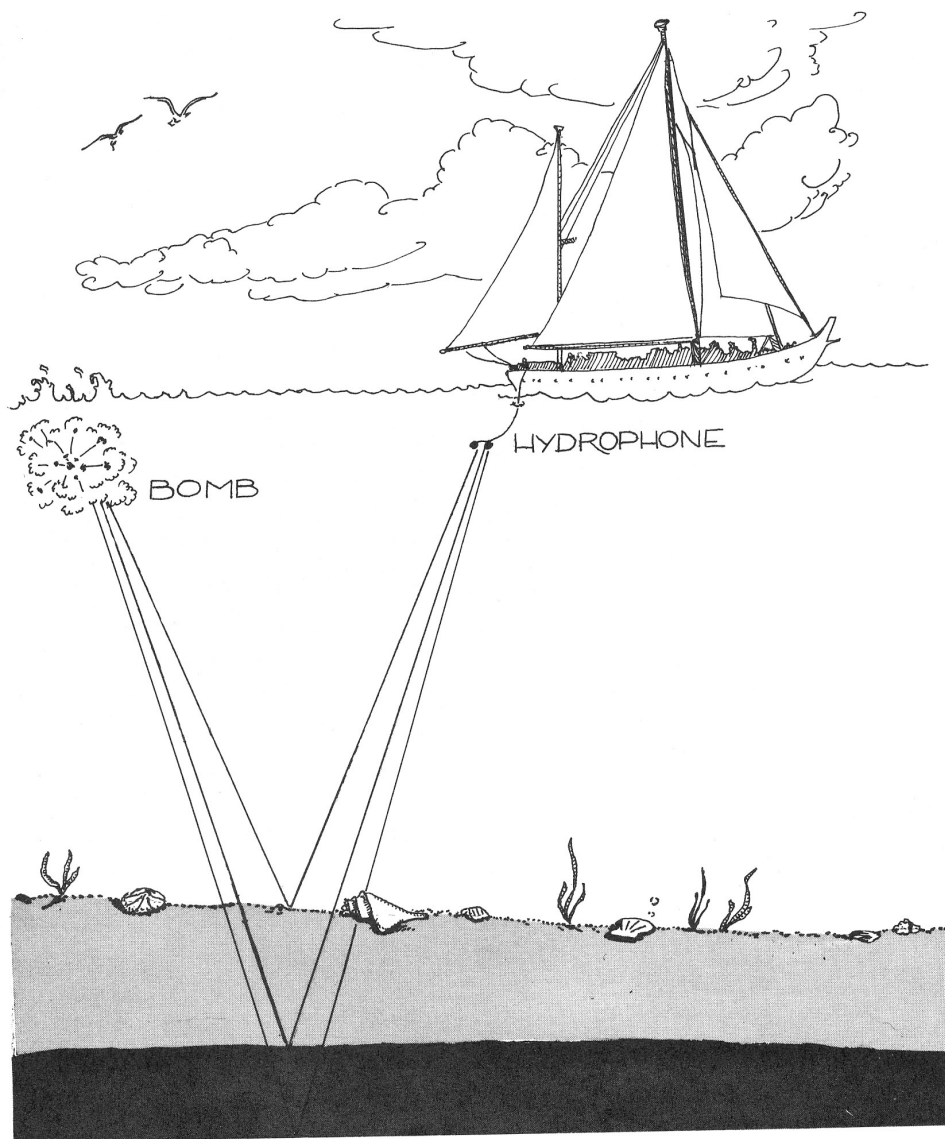
Explosion wave paths during seismic reflection.

Seismic shooting went on at half-hour intervals.

Zero-offset VSP

Source

Downgoing multiple — Time →

Direct wave

Receiver position

Reflected primary

Reflected upgoing multiple

Subsurface reflector

North

z

y

x
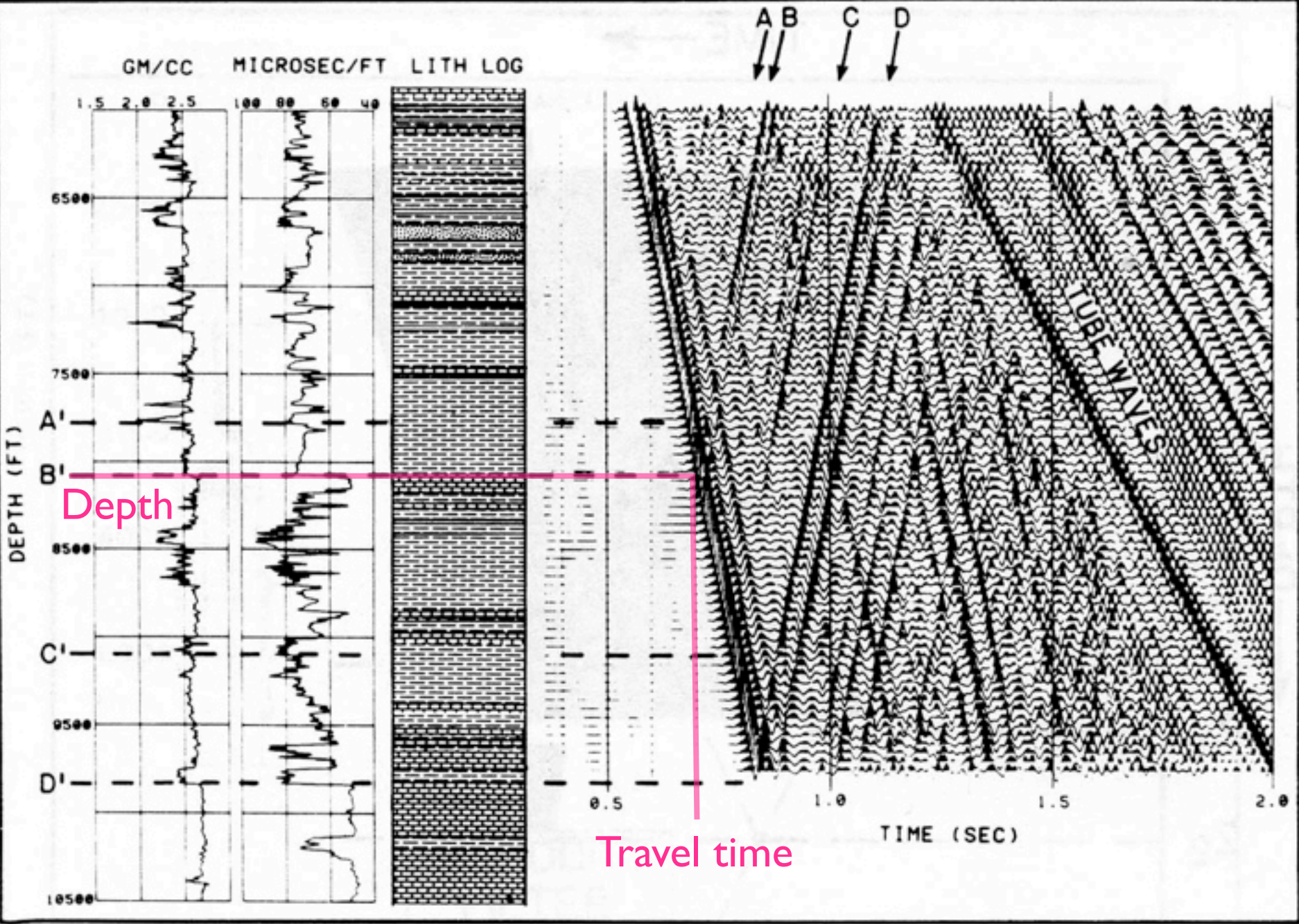
After Hardage (1985)

- Nuclear Logs
- Sonic
- Electrical / magnetic
- Imaging
- Vertical seismic profile (VSP)
- Logging While Drilling
- Examples

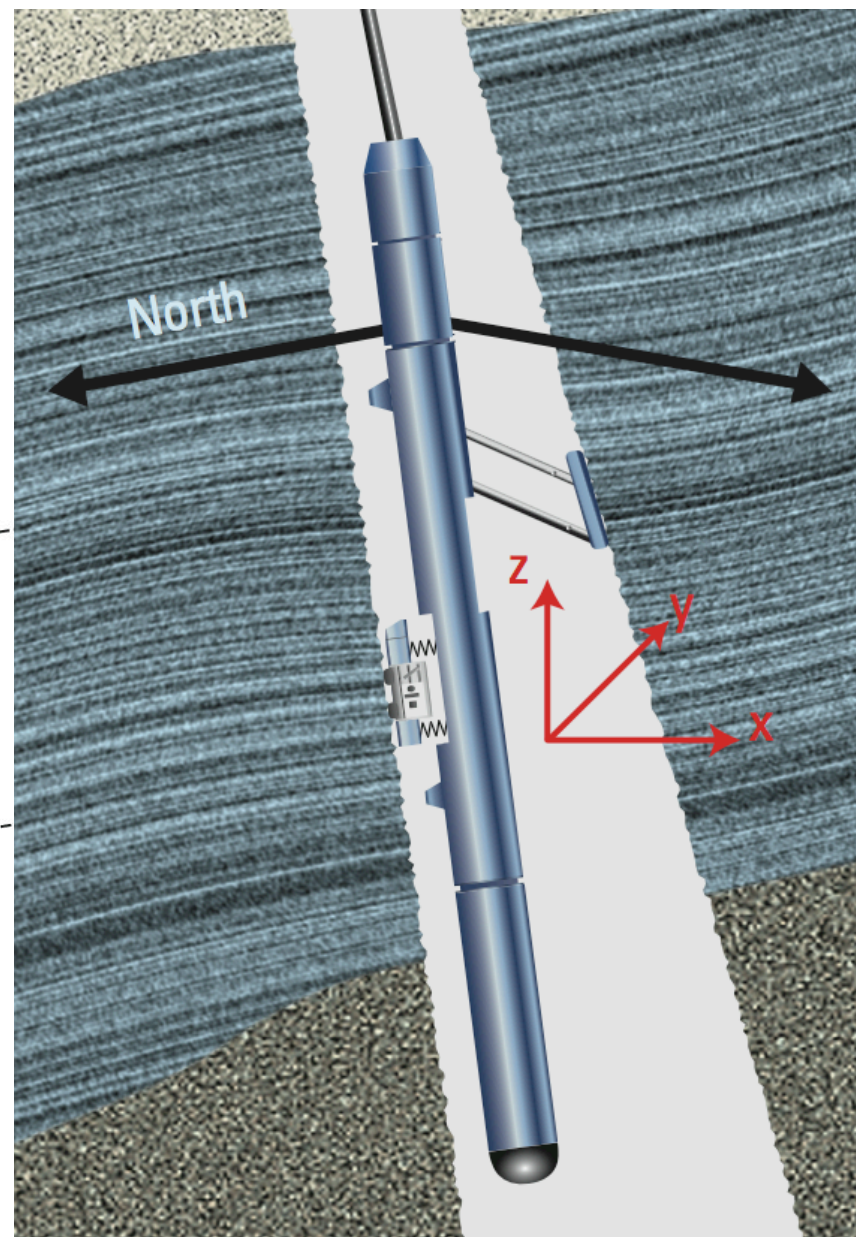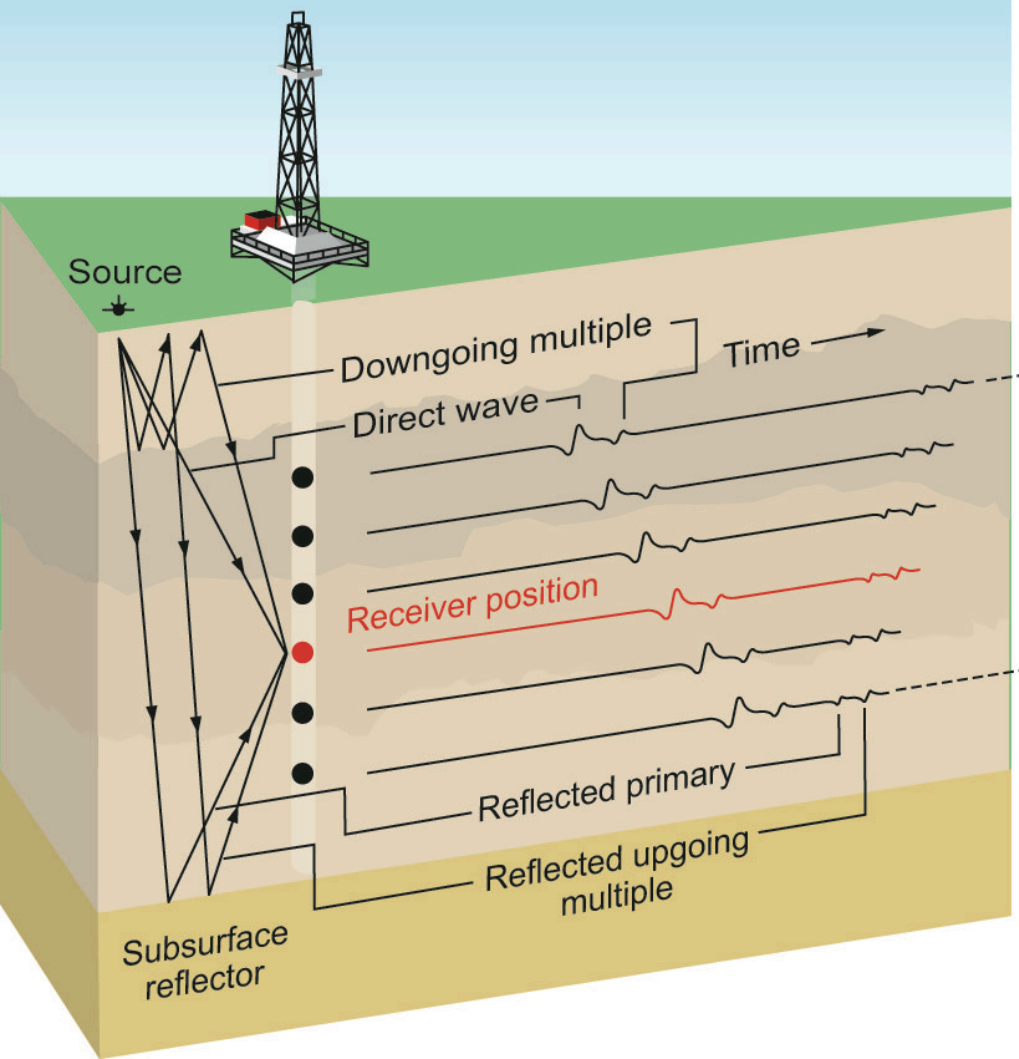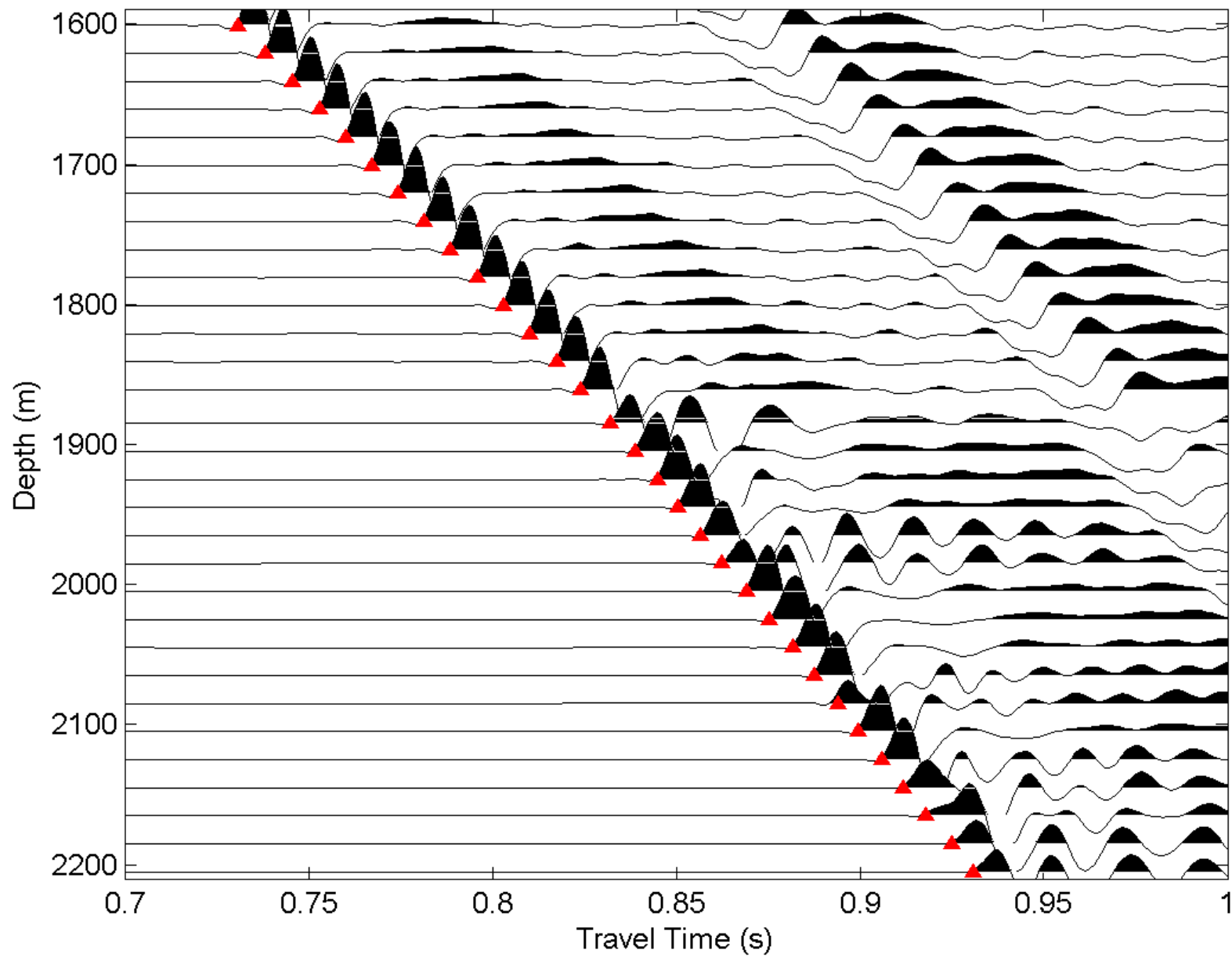Wireline logging

Logging while drilling (LWD)

Distance above bit (m)

Label	Distance
adnVISION	45.73
	39.71
proVISION (NMR)	
	28.43
Telescope (MWD)	
	20.04
	17.7 Sonic array
SonicVISION	
	12.51
Ecoscope	
	6.46 Pressure sensor
	5.62 Gamma ray sens
geoVISION (RAB)	4.46
Bit Sub	0.38
Bit	0.00

Crown block
Derrick
Heave compensator
Top drive
Cranes
Scientific lab stack
Berthing
Underway geophysics lab
Bridge
Helodeck
AFT
Pipe racker
Rig floor
Guide horn
FORE
Dynamic position thrusters
Drill string
Reentry cone
Seafloor
Drill bit
Casing

Upper transmitter

Azimuthal electrodes

Ring electrode

Lower transmitter

56 samples

RAB Image
Top   Bottom   Top

FMI Image
Top   Bottom   Top

Depth 10 ft

□RAB and FMI images of dipping beds. Both RAB and FMI images show large-scale events that are several feet long. However, the resolution of the FMI image is much better. Beds less than about 4 in. [10 cm] thick are not clearly seen on the RAB image.
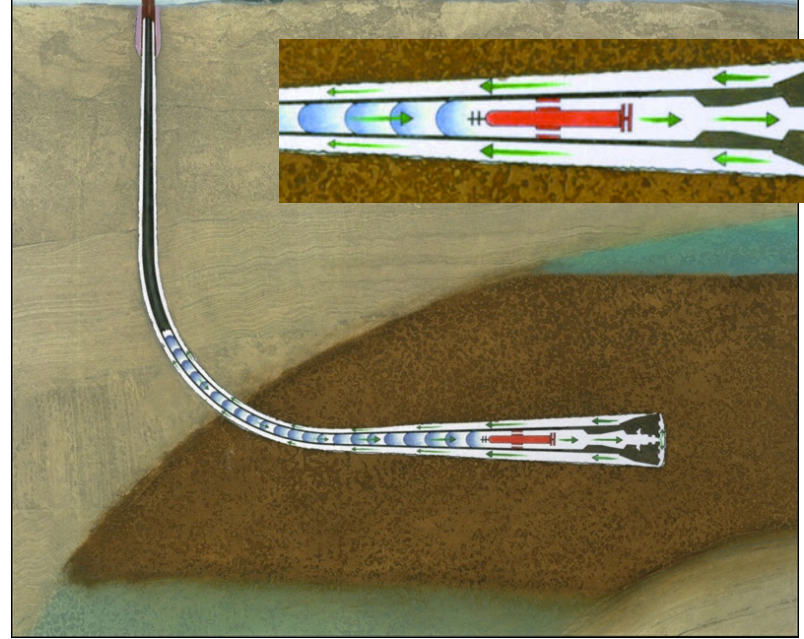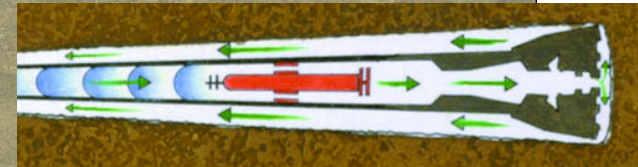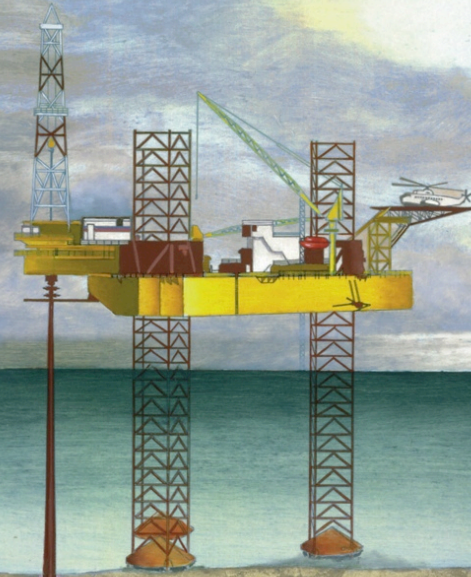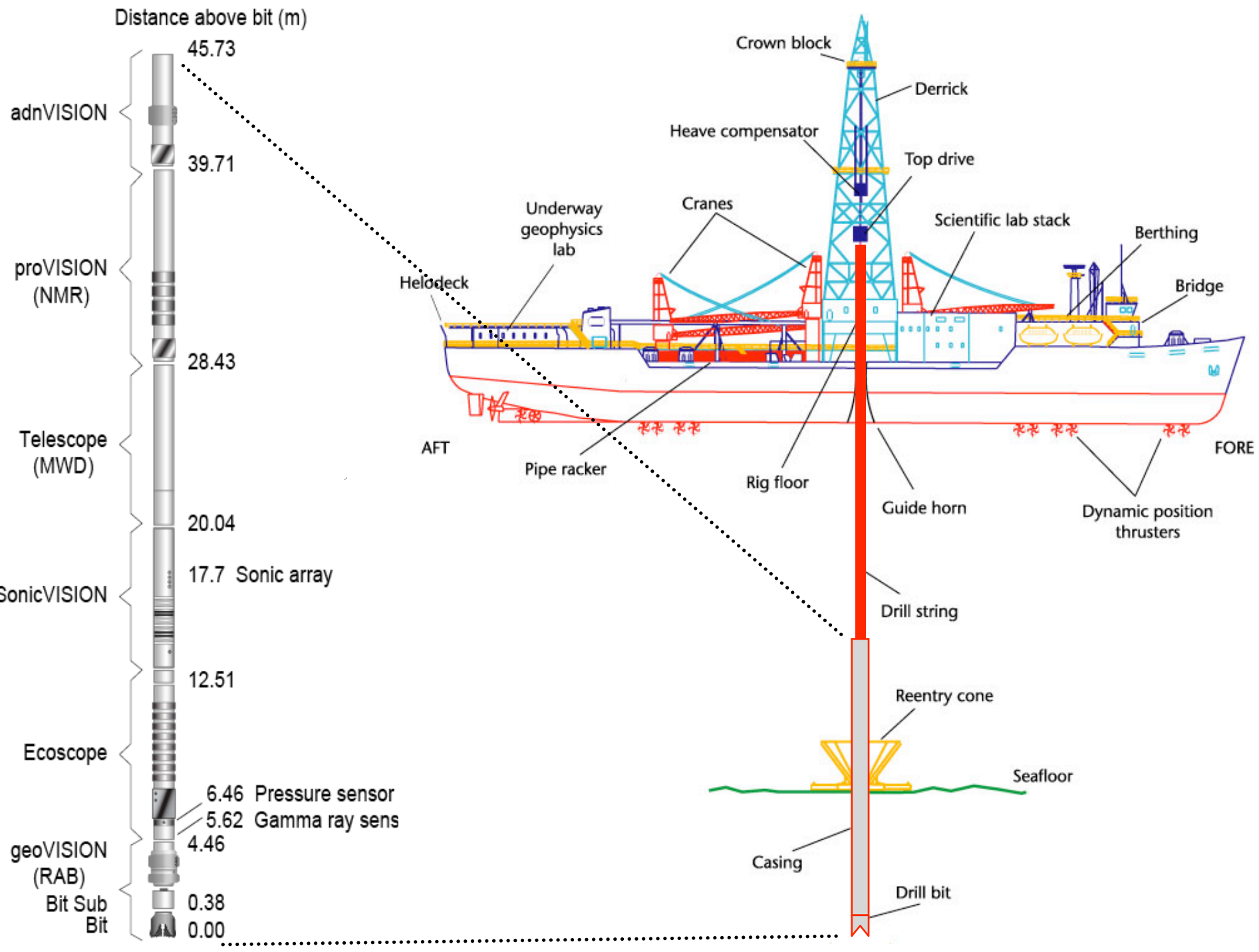
- Nuclear Logs
- Sonic
- Electrical / magnetic
- Imaging
- Vertical seismic profile (VSP)
- Logging While Drilling
- Examples

Hole-to-hole correlation
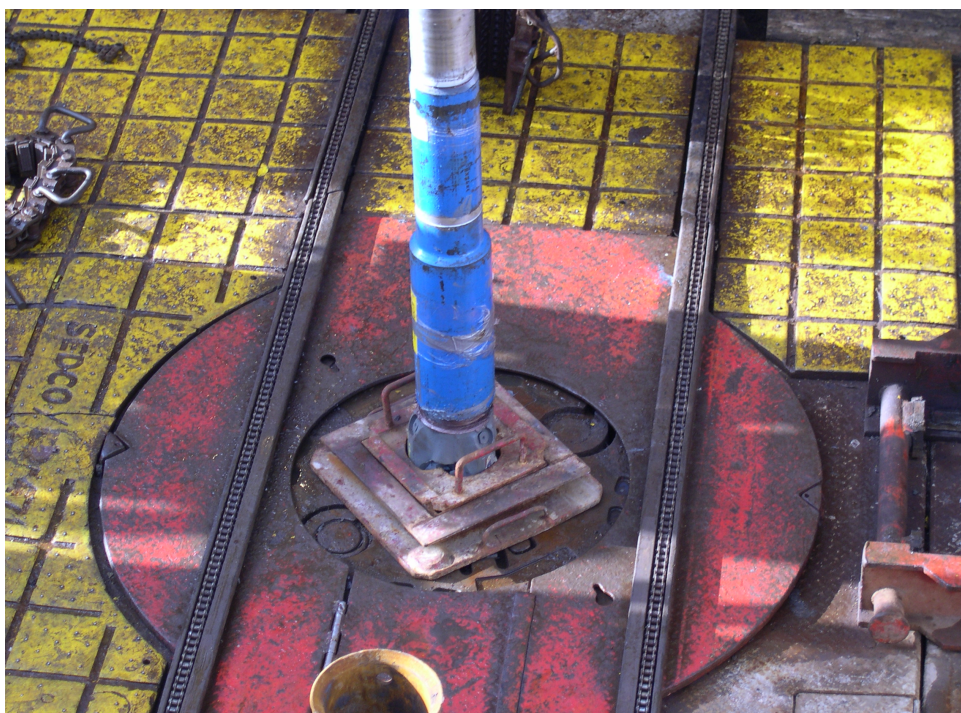

Figure F45. Downhole gamma radiation and resistivity logs from Holes 1207B and 1213B illustrating the form and setting of the Aptian Oceanic Anoxic Event (OAE1a) black shale.
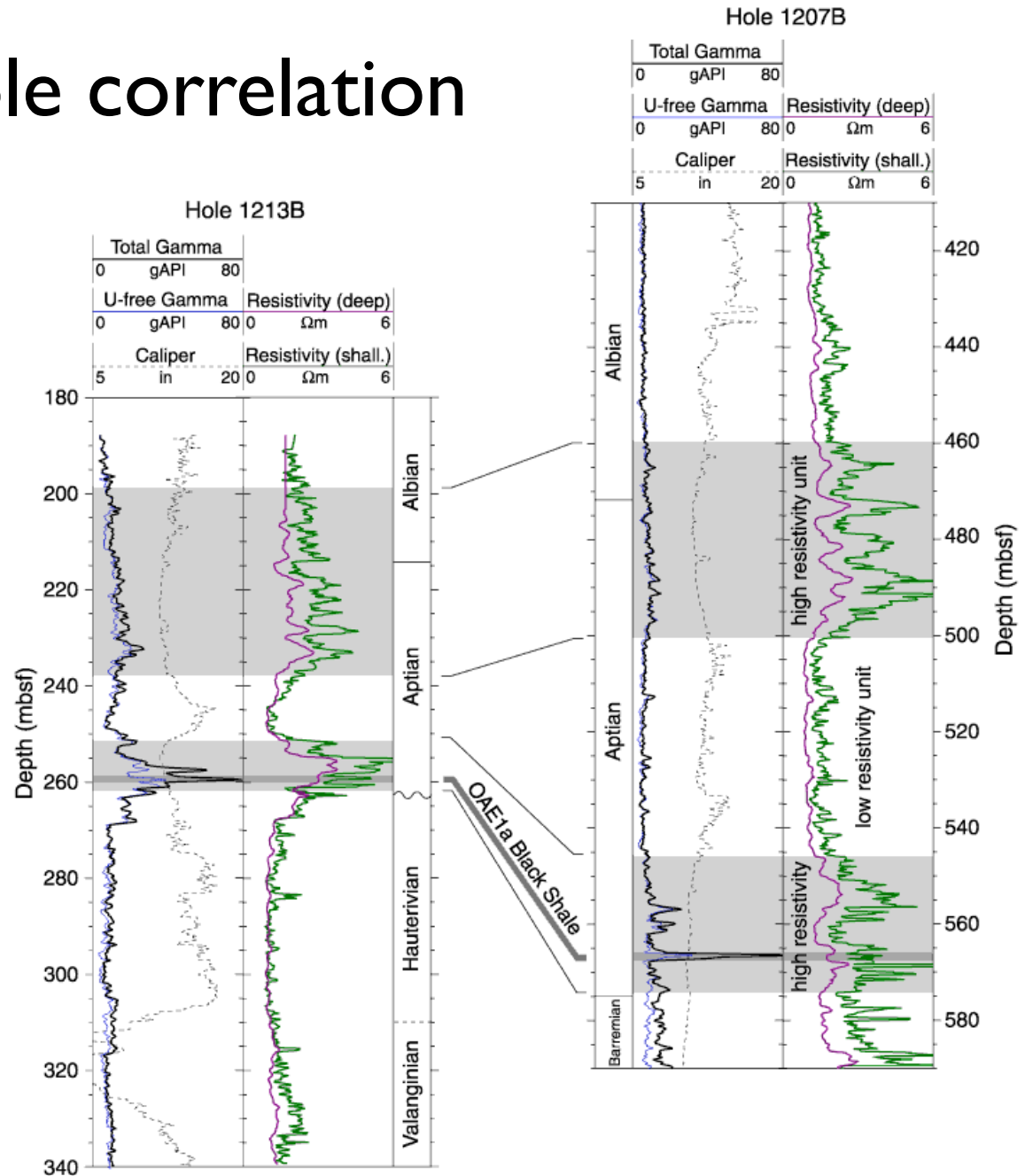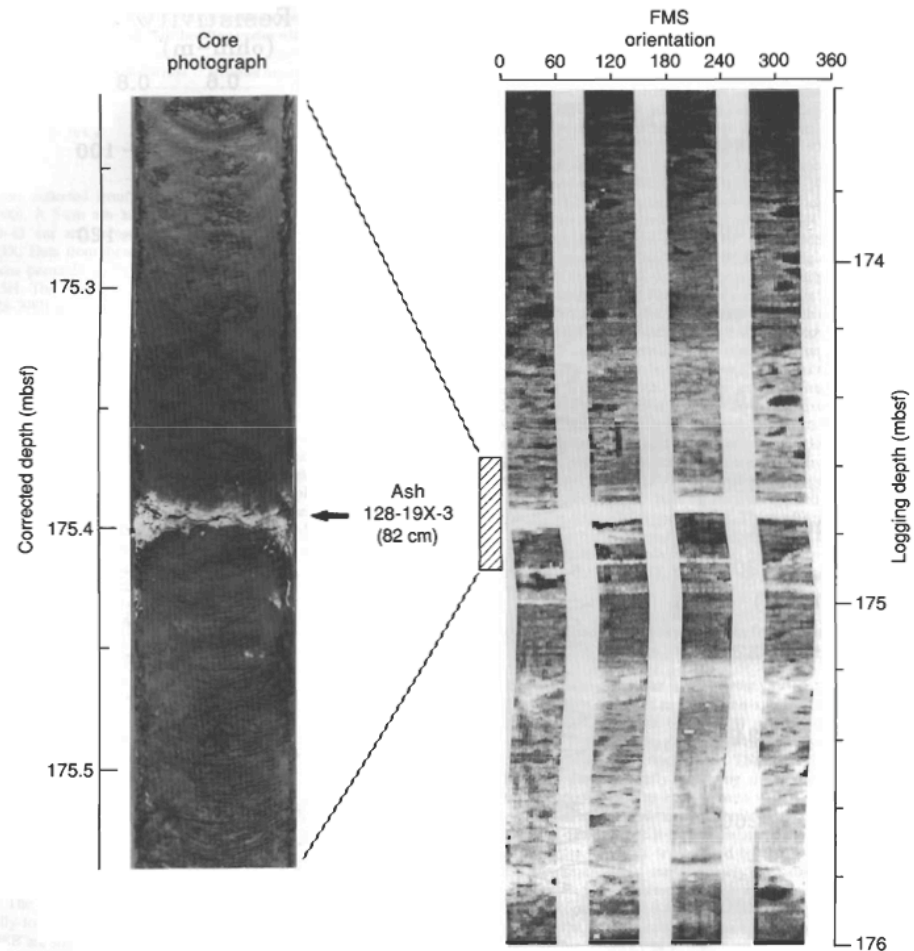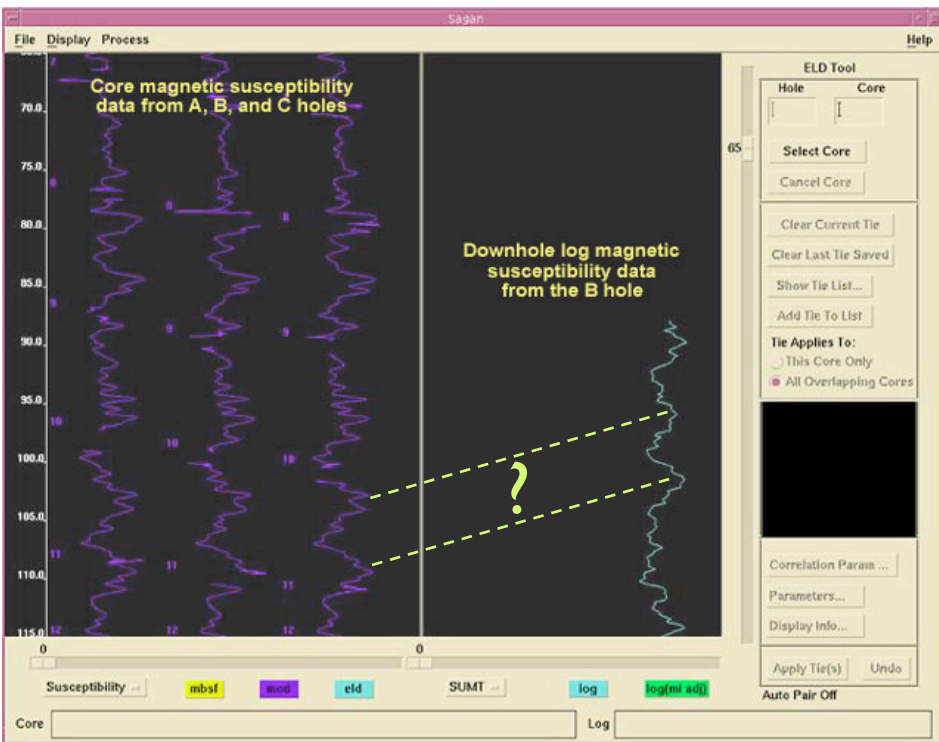
Figure 8. Example of core-log correlations using volcanic ashes. Core photograph is of ash layer in Core 128-798B-19X-3 (82 cm) at 175.40 mbsf (depths corrected for core expansion). The formation microscanner (FMS) microresistivity images of this interval are shown at right. The images are azimuthal (0°–360° magnetic declination, left-to-right) traces of four orthogonal pads which are pressed against the borehole wall. The ash layer appears as a bright (highly resistive) band at a 174.70 mbsf logging depth.

Hole 798B

Gamma Ray (SGR)
(API units)

Resistivity
(ohm-m)

Bulk Density
(g/cm³)

Opal
(%)

Carbonate
(%)

Terrigenous
(%)

Actual core data (━━)

Predicted from logs (——)

Site 607 δ¹⁸O (‰) ($\longleftrightarrow$)

Glacial ◄———► Interglacial

Age
(M.Y.)

Site 798B gamma-ray (····)

◄ increasing
terrigenous
content
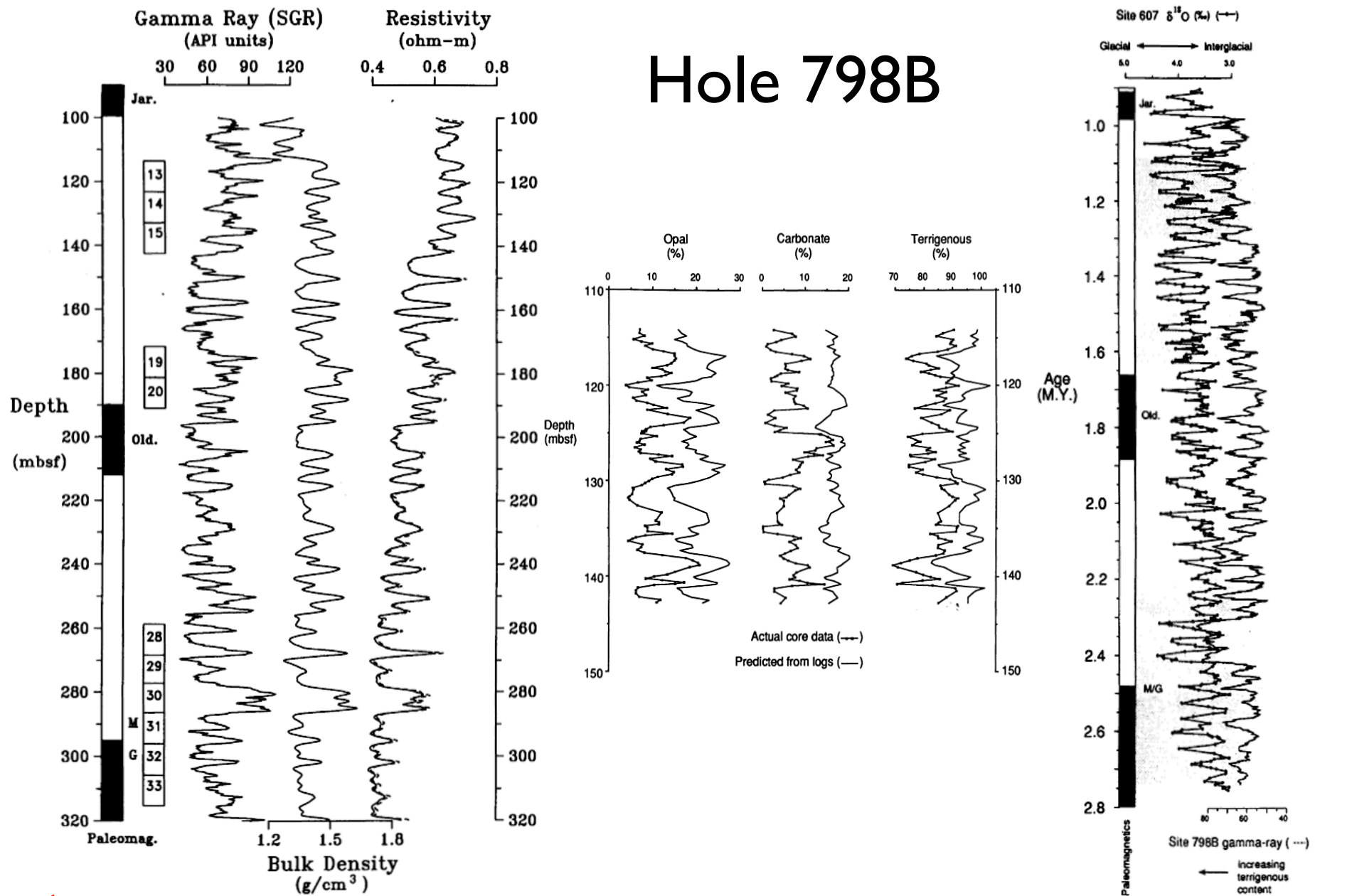
Opal from diatoms
(Glacial)

Terrigenous material
(Interglacial)

Figure 14. Correlation of the Hole 798B SGR gamma-ray log with the marine δ¹⁸O record from Site 607 in the North Atlantic (Raymo et al., 1989; Ruddiman et al., 1989). The SGR time series was initially constrained using the paleomagnetic reversal boundaries. Minor adjustments to the SGR time series were performed using the CORPAC correlation program to improve its alignment with the Site 607 δ¹⁸O record. The age-depth plot resulting from this process is shown in Figure 15.
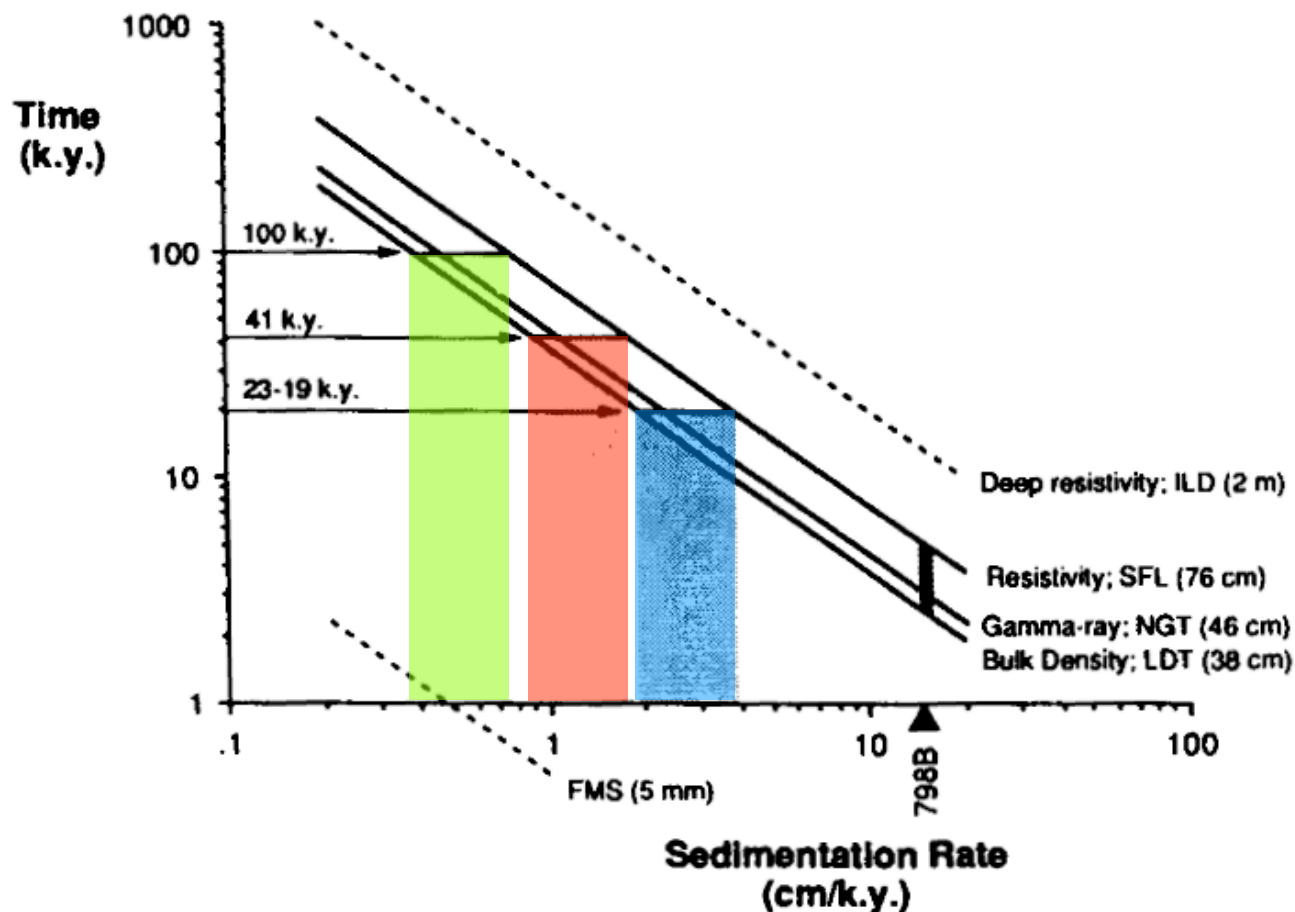
Figure 5. Plot of the temporal resolution of several logging tools as a function of sedimentation rate. Temporal resolution was calculated as vertical aperture/sedimentation rate. Minimum sedimentation rates required to resolve 100 k.y., 41 k.y., and 23–19 k.y. in time are shown as shaded columns. Note that these sedimentation rates are only sufficient to resolve a time interval (Δt) equivalent to 100 k.y., 41 k.y., and 20 k.y.
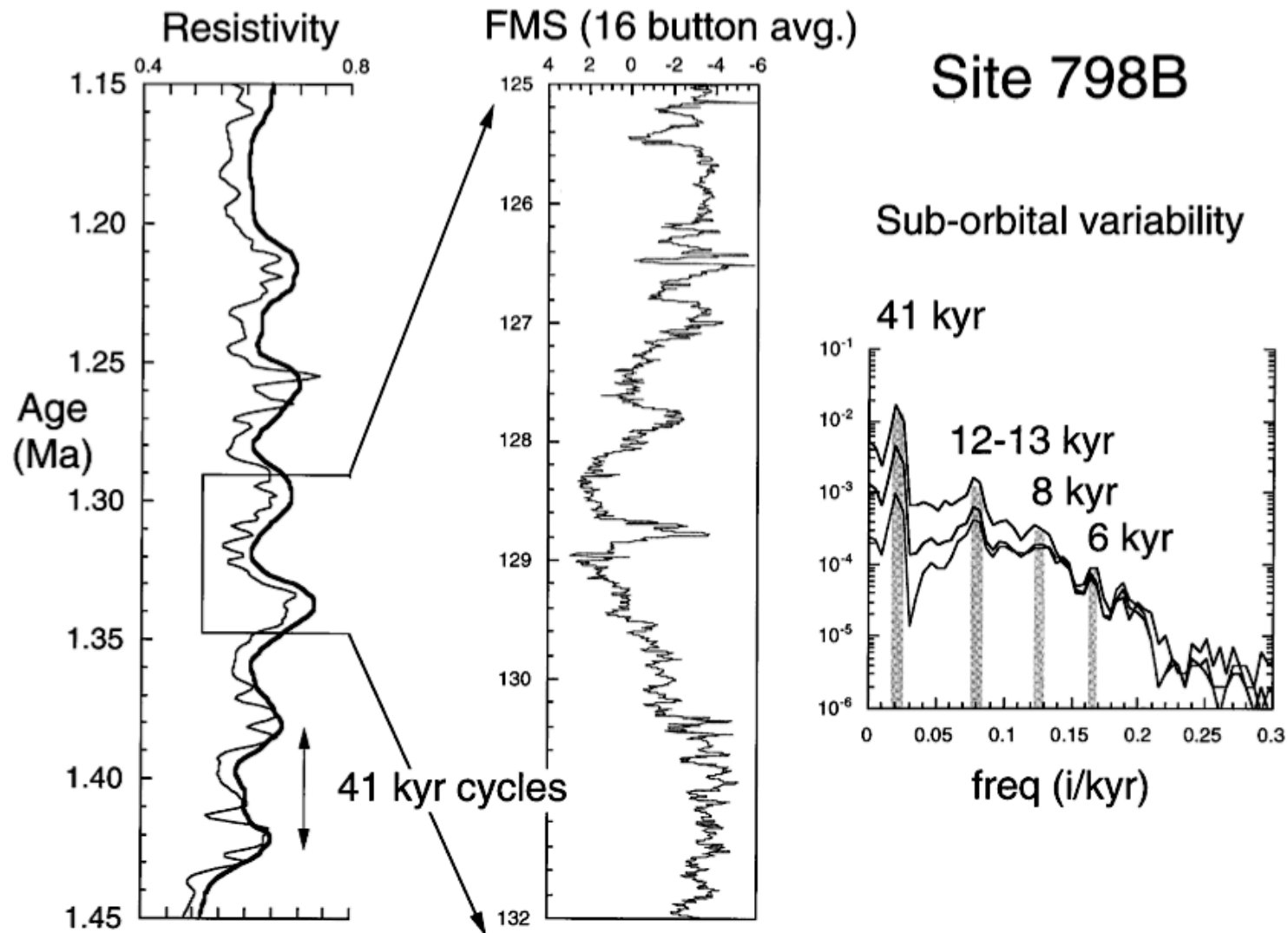
Figure 9. Comparison of data from three wireline resistivity tools: shallow and deep resistivity and the averaged FMS record that show cycles at a 41,000-year orbital period and below in the comparative power spectra [after *deMenocal and King*, 1995]. The resistivity logs have been converted to age, and the averaged FMS data are plotted on relative scale over a 7-m interval. The fine vertical resolution of the FMS data allows observation of periods as short as 6000 years.
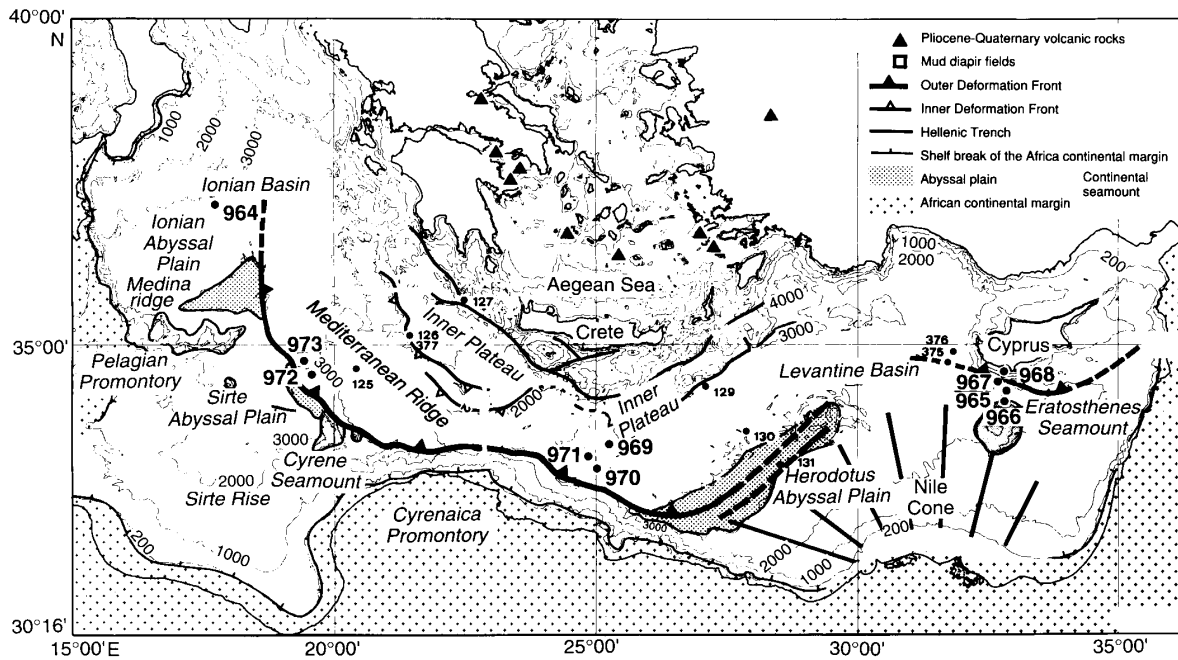
Figure 1. Outline map of the Mediterranean showing the main tectonic features and location of the sites drilling during Leg 160. DSDP sites are also shown.
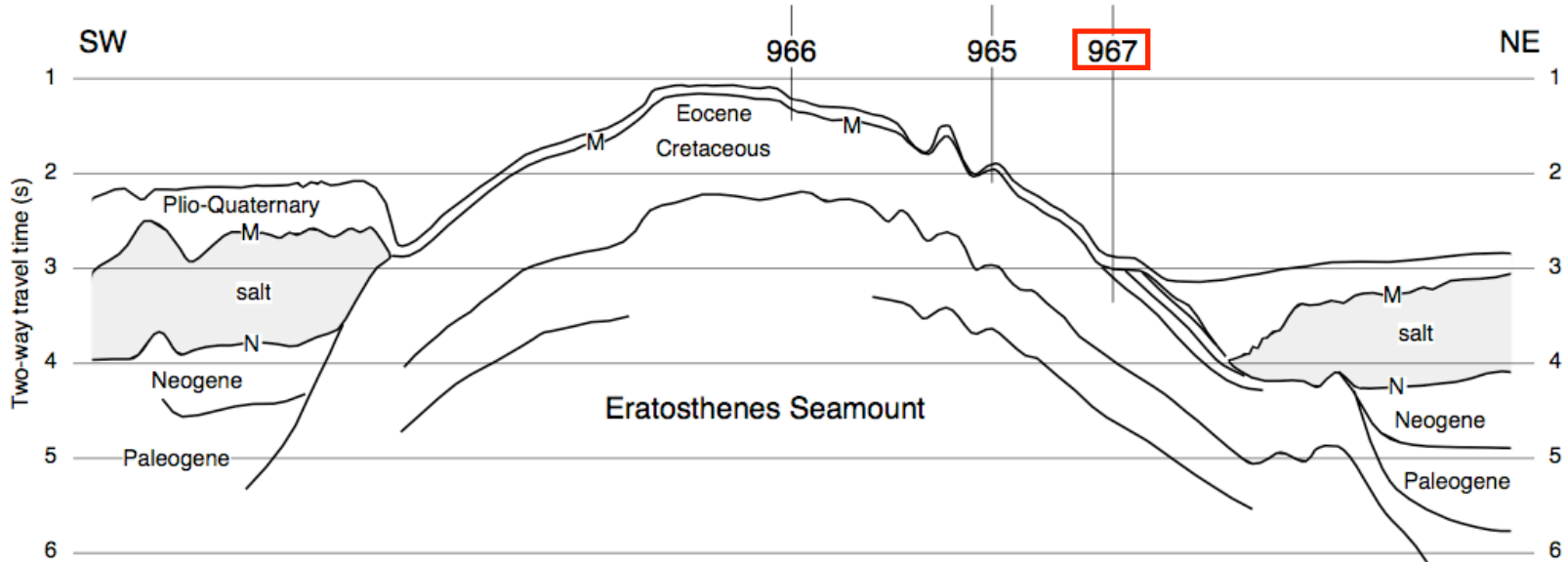

Figure 3. Interpreted multichannel seismic profile 10 (see Fig. 2 for location) extending across the Eratosthenes Seamount, illustrating the thick accumulations of Neogene and Paleogene sediments in the adjacent basin. The drill sites are projected onto the profile. Note that the seamount comprises mainly Cretaceous and older strata.
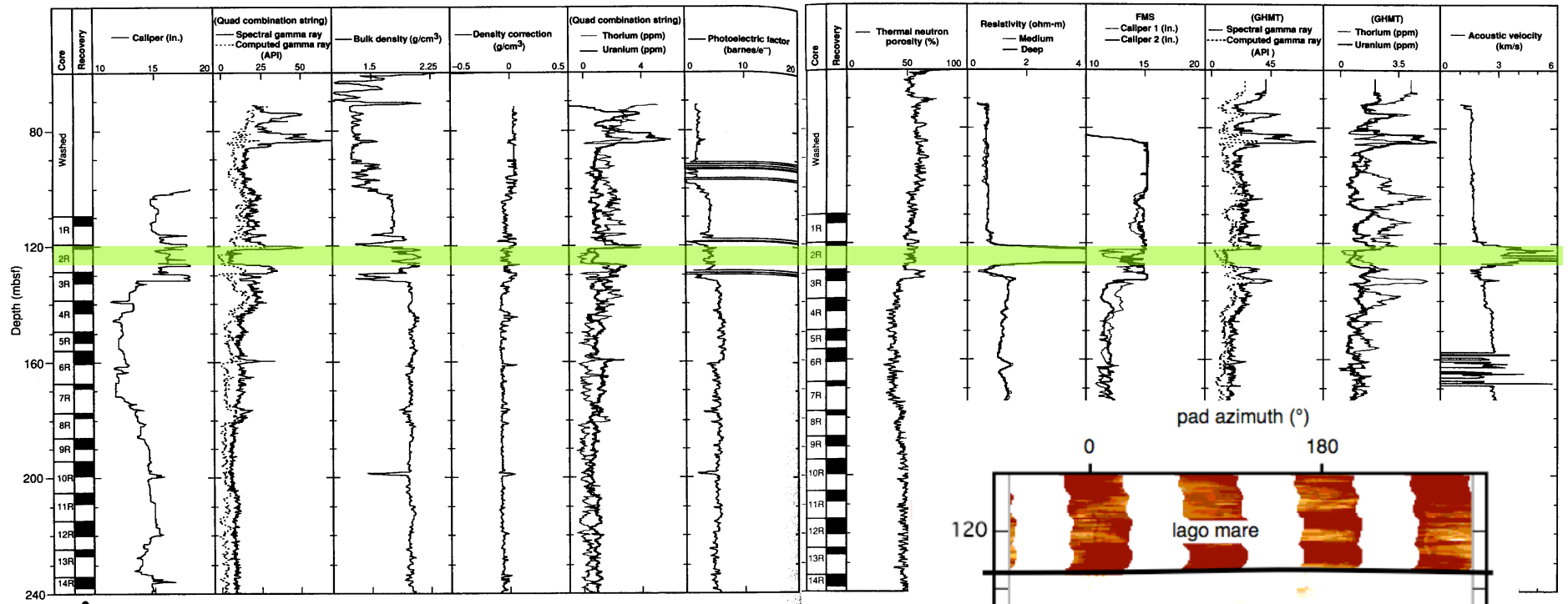
Figure 63. Hole 967E Quad combination tool and FMS (4-arm) caliper results.

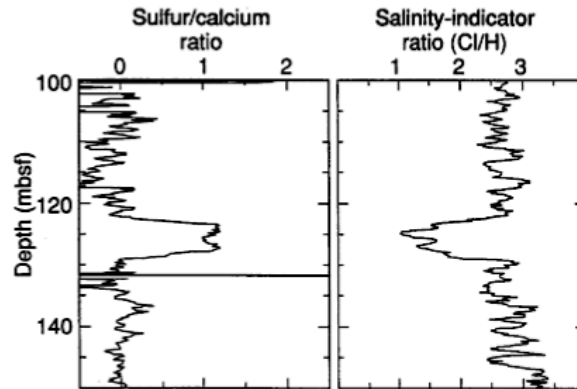Hole 967E average core recovery 15%

Figure 18. Example of a 4-m-thick layer with high sulfur/calcium and low chlorine/hydrogen ratios from the geochemical log, identifying it primarily as gypsum in ODP Hole 967C in the eastern Mediterranean Sea [from *Emeis et al.*, 1996]. The logs provided critical data in identifying this early basin deposit that was not recovered during coring operations.
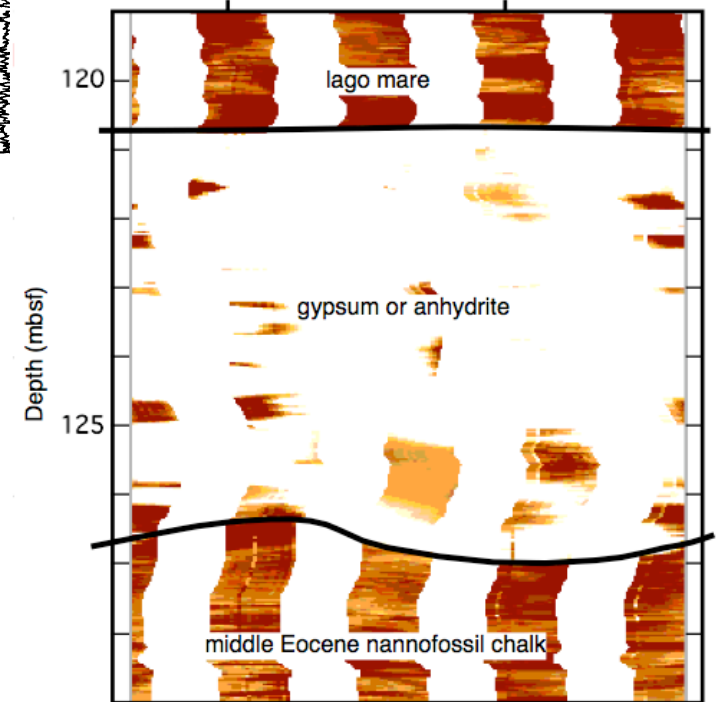

Figure 15. FMS image of the ~5-m-thick gypsum layer overlying upper Eocene foraminiferal nannofossil chalk. This erosional unconformity is quite irregular on a small spatial scale.